

Impact of faults on the remote stress state

Karsten Reiter¹, Oliver Heidbach^{2,3}, and Moritz. O. Ziegler^{2,4}

¹Institute of Applied Geosciences, TU Darmstadt, 64287 Darmstadt, Germany

²Helmholtz Centre Potsdam, GFZ German Research Centre for Geosciences, 14473 Potsdam, Germany

³Institute of Applied Geosciences, TU Berlin, 10587 Berlin, Germany

⁴TU Munich, 80333 Munich, Germany

Correspondence: Karsten Reiter (reiter@geo.tu-darmstadt.de)

Abstract.

The impact of faults on the contemporary stress field in the upper crust has been discussed in various studies. Data and models clearly show that there is an **impacteffect**, but so far, a systematic study ~~that quantifies~~ quantifying the impact as a function of distance ~~to from~~ the fault is ~~missing. As there is a lack of dense data, we use here~~ lacking. In the absence of
5 data, here we use a series of generic 3-D-models to investigate which component of the ~~3-D-stress~~ stress tensor is affected at ~~what distance to~~ which distance from the fault. Our ~~focus is~~ study concentrates on the far-field~~beyond hundreds of meters,~~ located hundreds of metres from the fault zone. The models ~~test different approaches to implement~~ assess various techniques to represent faults, different material properties, different boundary conditions, variable orientation, and ~~size of the fault. The results of our study show that beyond 1.000~~ the fault's size. The study findings indicate that most of the factors tested do not
10 have an influence on either the stress tensor orientation or principal stress magnitudes in the far field beyond 1000 m ~~distance to the fault, the displacements along the fault and its strength contrast neither leaves an imprint on the orientation of the stress tensor nor in the magnitude of the principal stresses in the far field~~ from the fault. Only in the case of oblique faults with low static friction coefficient of $\mu = 0.1$, noteworthy stress perturbations can be seen up to 2000 m from the fault. However, the changes that we detected are generally small an in the order of lateral stress variability due to rock property variability.
15 Furthermore, only in the first 100's of meters distance to the fault variations are large enough to be theoretically detected by borehole based stress data when considering their inherent uncertainties. This finding agrees with robust ~~data from either~~ stress magnitude measurements ~~or and~~ stress orientation data. Thus, in areas where high-quality and high-resolution data ~~on the change in orientation of the stress tensor are available. The latter shows often continuous and gradual rotation of the stress tensor orientation~~ show a gradual and continuous stress tensor rotations of $> 20^\circ$ are observed over lateral spatial scales of
20 10 km or ~~larger. These more we infer that these~~ rotations cannot be attributed to faults~~as they only have an impact on scales < 1 km down to several meters only, as observed in numerous boreholes. Thus, we postulate.~~ We hypothesise that most stress orientation changes ~~that are assigned~~ attributed to faults may ~~have a different source.~~ originate from different sources such as density and strength contrasts.

The crustal stress field is a key driver of geodynamic processes such as the earthquake cycle (Brodsky et al., 2020; Hardebeck and Okada, 2007; Heidbach and Ben-Avraham, 2007; Wang et al., 2015; Hardebeck and Okada, 2018; Brodsky et al., 2020) and is of great importance for the safe exploitation of georeservoirs and storage of energy or waste in the subsurface (Fuchs and Müller, 2001; Smart et al., 2001; Fuchs and Müller, 2001; Zoback, 2010; Smart et al., 2014). In this context the interaction between the stress field in the Earth's upper crust and pre-existing faults is a crucial issue (Blöcher et al., 2018; Kruszewski et al., 2022; Li et al., 2023; Röckel et al., 2022; Schoenball and Davatzes, 2017; Blöcher et al., 2018; Kruszewski et al., 2022; Röckel et al., 2022; Li et al., 2023).

For practical applications it is important, to understand and to quantify on which spatial scale the fault changes the stress state. Exemplified on the site selection process for a deep geological repository for high-level radioactive waste, the interest is to know the distance to a fault at which no significant changes of the stress components occur in order to build the repository in a rock volume with homogeneous stress field conditions. In contrast to this, deep geothermal exploration targets faults or fault networks since they provide higher permeability's-permeabilities compared to the rock matrix. Thus, the changes of the stresses in the near-field of the fault and in its core or fracture network is of key interest to assess its dilation tendency (Ferrill et al., 2020; Moeck and Baekers, 2011; Seithel et al., 2019). (Moeck and Baekers, 2011; Seithel et al., 2019; Ferrill et al., 2020)

. Stress perturbations are also significant for evaluating secondary fracturing near faults and its associated permeability, which encompasses joint orientation, secondary faulting, and bed-parallel slip (e.g. Kattenhorn et al., 2000; Maerten et al., 2002; Delogkos et al., 2002).

One of the key questions is, on what spatial scale faults change the stress field and to quantify which stress components are affected. The only component of the 3-D stress tensor that is systematically compiled is the orientation of maximum horizontal stress (S_{Hmax} , Heidbach et al., 2004, 2018)(S_{Hmax} , Heidbach et al., 2004, 2018). Areas with high data density revealed that the S_{Hmax} S_{Hmax} orientation can rotate significantly on scales from 10's to 100's of kilometres (Heidbach et al., 2018, 2007; Lund Snee and Zoback, 2006; Tingay et al., 2006; Heidbach et al., 2007; Rajabi et al., 2017b; Heidbach et al., 2018; Lund Snee and Zoback, 2020). The cause of this spatial variability has been investigated with generic geomechanical-numerical and analytical modelling (e.g. Reiter, 2021; Sonder, 1990; Sonder, 1990; Reiter, 2021). These studies show that stiffness, strength and density contrasts are certainly a key driver of spatial distributed changes of the S_{Hmax} S_{Hmax} orientation.

The general structure

Besides these findings, it was also hypothesised that active faults can cause rotations or magnitude variations as well (Dart and Swolfs, 1992; Faulkner et al., 2006; Konstantinovskaia et al., 2012; Li et al., 2023; Schoenball et al., 2018; Yale, 2003) (Dart and Swolfs, 1992; Yale, 2003; Faulkner et al., 2006; Konstantinovskaia et al., 2012; Schoenball et al., 2018; Li et al., 2023)

. This is confirmed on borehole scale since logging data show stress rotations on the meter scale by means of abrupt changes in the orientation of borehole breakouts and drilling induced tensile fractures (e.g., Barton and Zoback, 1994; Rajabi et al., 2017c) -This was also observed in the scientific SAFOD borehole, drilled through the San Andreas fault (Zoback et al., 2011). (e.g., Barton and Zoback, 1994; Zoback et al., 2011; Rajabi et al., 2017c). It clearly showed that there are indeed stress rota-

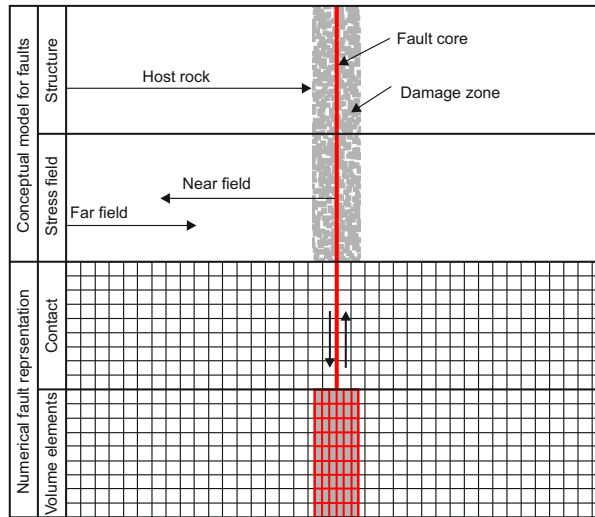


Figure 1. The general structure of a fault is described by the fault core, the damage zone, and the host rock (e.g., Caine et al., 1996; Faulkner et al., 2003). The purpose of this study is not to explore the effect of a fault on the stress state in the near field. This would include the fault core, the damage zone, and the neighbouring host rock. The study is focused on the far-field stress state, which is located several tens or hundreds of metres away from the fault and can extend up to a few kilometres at most. Numerical models typically employ one or a combination of two principle technical fault representations. Contact surfaces are a discontinuity within the mesh, where relative offset of the mesh is allowed, mainly depending on the friction. The second method use a continuous mesh with elements having a lower stiffness or a failure criterion which results in a distributed deformation within the defined fault representation elements.

tions on scales of one to several hundreds of meters occur, due to faults and that the amount of rotation changes with distance to the fault core (Hickman and Zoback, 2004). Significant variation of stress magnitudes in the vicinity of faults has been reported for China and Scandinavia (Li et al., 2023; Stephansson and Ångman, 1986)(Stephansson and Ångman, 1986; Li et al., 2023), but from these studies it is not clear which stress tensor component is affected as a function of distance to the fault. Furthermore, the mix of different methods that are used to estimate stress parameter from very shallow locations near surface as well as the lack of a rigorous uncertainty assessment makes it difficult to assess whether the observed changes are significant and if they can be exclusively attributed to the nearby fault.

List of some example studies, using either a continuous or discontinuous mesh as fault representation (Fig. 1). Discontinuities are represented by contact elements or comparable methods (Contact). Another way to represent faults is a continuous mesh having a somehow weaker material definition (elastic, plastic or viscous). These are 2-D elements within a 2-D Mesh or 3-D Elements in a 3-D mesh (Volume). Many models apply the Finite Element Method (FEM), others use the Finite Difference Method (FDM), Finite Volume Method (FVM), the Discrete Element Method (DEM). (The list does not claim to be complete.) Authors Contact Volume Tommasi et al. (1995) x Buchmann and Connolly (2007) x Xing et al. (2007) x Hergert et al. (2011) x Reiter and He x Pereira et al. (2014) x Hergert et al. (2015) x Franceschini et al. (2016) x Zhang et al. (2016) x Meier et al. (2017) x Schuite et al. (2017)

Table 1. List of a fault is described by the fault coresome studies, exemplifying the damage zone, and the host rock (e.g., Caine et al., 1996; Faulkner et al., 2003). The aim use of the work is not to investigate the impact of either a continuous or discontinuous mesh for fault on the near field stress state representation (Fig. This would include the fault core, the damage zone, and the neighbouring host rock 1). The focus-Discontinuities are represented by contact elements or comparable methods (Contact). Another method of this study modelling faults is on the far field stress state, which is away from the fault of about utilising a few tens continuous mesh that possesses a material definition slightly or hundred metressignificantly weaker (elastic, to a maximum of a few kilometres. Numerical models usually use one plastic or a combination of two principle technical fault representationsviscous). Contact surfaces-These are a discontinuity 2-D elements within the a 2-D Mesh or 3-D Elements in a 3-D mesh (Volume). Many models apply the Finite Element Method (FEM), where relative offset of others use the mesh is allowedFinite Difference Method (FDM), mainly depending on Finite Volume Method (FVM), the frictionDiscrete Element Method (DEM). (The second method use a continuous mesh with elements having a lower stiffness or a failure criterion which results in a distributed deformation within the defined fault representation elementslist does not claim to be complete.)

	<u>Authors</u>	<u>Contact</u>	<u>Volume</u>
Finite Element Method	<u>Tommasi et al. (1995)</u>	-	x
	<u>Buchmann and Connolly (2007)</u>	x	-
	<u>Xing et al. (2007)</u>	x	-
	<u>Hergert et al. (2011)</u>	x	-
	<u>Reiter and Heidbach (2014)</u>	x	-
	<u>Pereira et al. (2014)</u>	-	x
	<u>Hergert et al. (2015)</u>	x	-
	<u>Franceschini et al. (2016)</u>	x	-
	<u>Zhang et al. (2016)</u>	-	x
	<u>Meier et al. (2017)</u>	-	x
	<u>Schuite et al. (2017)</u>	-	x
	<u>Trefffeisen and Henk (2020b)</u>	x	x
	<u>Reiter (2021)</u>	x	-
other methods	<u>Homberg et al. (1997)</u>	x	-
	<u>Sánchez D. et al. (1999)</u>	x	-
	<u>Maerten et al. (2002)</u>	x	-
	<u>McLellan et al. (2004)</u>	-	x
	<u>Camac and Hunt (2009)</u>	x	-
	<u>Cappa (2009)</u>	-	x
	<u>Cappa and Rutqvist (2011)</u>	x	-

~~-xTrefffeisen and Henk (2020b)xxReiter (2021)x-Homberg et al. (1997)x-Sánchez D. et al. (1999)x-McLellan et al. (2004)-xCamac and H
x-Cappa (2009)-xCappa and Rutqvist (2011)x-~~

75 The only method to test ~~that this~~ are generic models, using ~~geomechnanical-geomechanical~~ numerical methods. There are several technical methods available to ~~mimie-represent~~ faults or fault zones numerically; for method overview see Henk (2020).

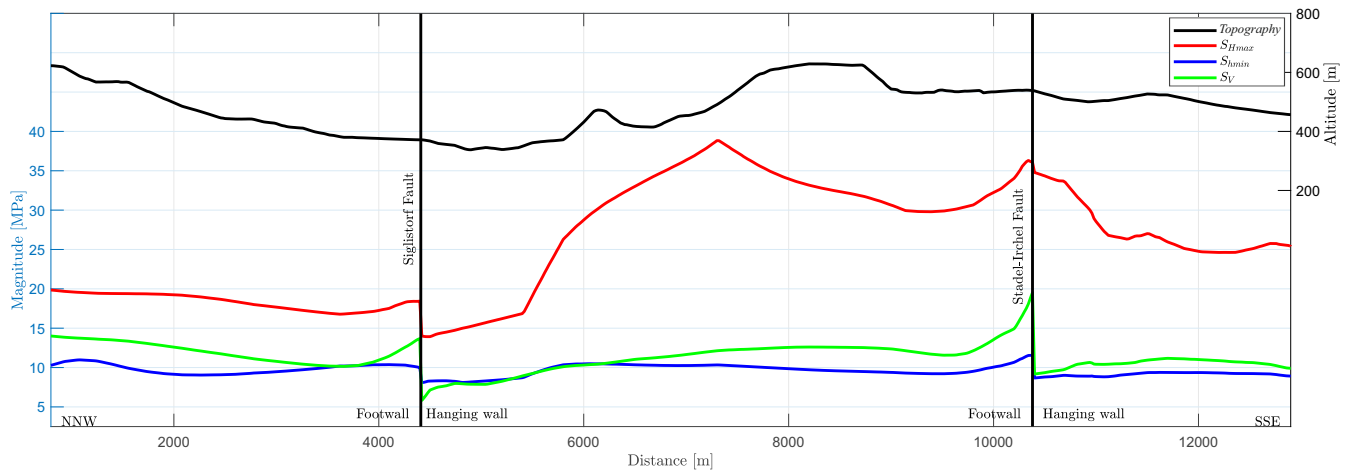


Figure 2. Plot of stress components along a NNW-SSE profile at approximately 400 m true-vertical depth (sea level) within the Nördlich Lägern model (Hergert et al., 2015). The largest and smallest horizontal principal stress (S_{Hmax} S_{Hmax} and S_{Hmin} S_{Hmin}), the vertical stress (S_V S_V) and the von-Mises stress are shown. Additional shown is the topography from the model. The location of the implemented Siglistdorf- and Stadel-Irchel fault are indicated by black vertical lines. Stress magnitudes changes are significant next to the fault faults, but they stresses are even more also variable due to a variable topography, rock stiffness or other factors. The significant variation in S_{Hmax} is attributed to material changes, as the stratigraphic boundaries dip slightly towards the south.

Where using the continuum method, a fault is represented by selected elements with different behaviour, e.g., a lower Young's modulus (e.g., Cappa and Rutqvist, 2011), a plastic behaviour (e.g., Mohr-Coulomb) or viscous behaviour. In contrast to that, using the discontinue method, the fault is represented by contact elements (e.g., Buchmann and Connolly, 2007; Hergert et al., 2015) which allow offset along these structures (Fig. 1, Tab. 1). The Finite Element Method (FEM) is often used for such studies. Another discontinue discontinuous method, where the geometry is divided into several individual elements (circles or spheres, etc.) is the Discrete Element Method (DEM, e.g., Cundall and Hart, 1992; Yoon et al., 2014), which will not be used here. Physical models, using a photo-elastic material (e.g. de Joussineau et al., 2003), are also an option.

The impact of faults has also been investigated by several authors using forward models. These studies (e.g. Tab. 1) either focus on how to technically implement faults into geomechanical-numerical models (Prévoist and Sukumar, 2016; Treffeisen and Henk, 2020b) or on specific geological settings (Chéry et al., 2004; Fitzenz and Miller, 2001; Hergert and Heidbach, 2011; Meier et al., 2017; Yoon et al., 2017). As an example, Fig. 2 plots stress components along a horizontal line at approximately 400 m true-vertical depth sea level within a model from northern Switzerland (Hergert et al., 2015). The magnitudes of the stress tensor vary significant close to the faults. However, resulting stress changes are affected by other factors too, such as topography or variable material properties etc.

Previous studies show that faults have certainly an impact, but a systematic approach is still missing. They do not provide a quantification, which component of the stress tensor is affected by the stress changes near the fault. In this paper we investigate systematically the change of individual stress tensor components with distance to the fault. In particular we determine the

changes of the ~~magnitudes of the~~ maximum and minimum horizontal stress (S_{Hmax} and S_{Hmin}), respectively, S_{Hmax} , S_{Hmin} , the vertical stress (S_V , S_Y) and the von Mises stress as well as the orientation of the stress tensor by means of the S_{Hmax} , S_{Hmin} azimuth in different settings regarding ~~fault~~ fault- and rock properties, stress regime and fault structure. Again, our focus is the far-field perspective, i.e. at distances ~~far~~ beyond 100 m from the fault core (Fig. 1). Thus, this work does not aim to answer the question to what extent the stress tensor components are affected in the near field.

2 Model set-up

100 2.1 Model concept

We set up generic 3-D models with model dimensions, rock properties and an initial stress state that are like the one from a 3-D geomechanical-numerical model of a potential siting area for a high-level radioactive waste disposal site in Northern Switzerland, presented by Hergert et al. (2015). For implementation in the model, faults are represented by contact elements, which allow an offset, or 3-D elements which are elastically or plastically weaker than the surrounding rocks (Fig. 1).

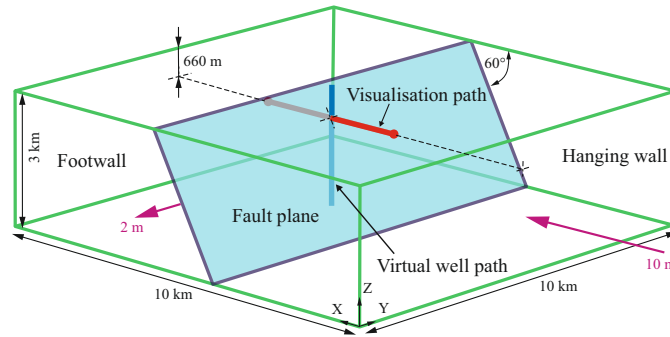


Figure 3. The model extent ($10 \times 10 \times 3 \text{ km}^3$, in green) with the fault (blue plane), inclined by 60° (dip angle), in red the visualisation path at a depth of 660 m along which the stress magnitudes are presented for the majority of the figures. The blue vertical line indicates the location of a virtual vertical borehole (Fig. 4). The displacement boundary conditions in purple are 10 m shortening ($\epsilon = -1 * 10^{-3}$) in X-direction (perpendicular to the strike direction of the fault), which governs the S_{Hmax} magnitude, and 2 m of dilation ($\epsilon = 2 * 10^{-4}$) in Y-direction (parallel to the strike direction of the fault), which drives the S_{Hmin} magnitude.

105 2.2 Partial differential equation and solution scheme

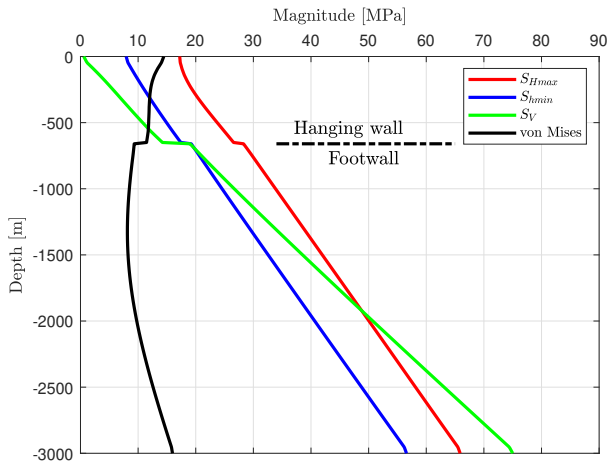
The two key components of a static stress state are a result from volume forces due to gravity and surface forces from plate tectonics. Neglecting acceleration, the resulting partial differential equation is the equilibrium of forces. For the upper crust assuming linear isotropic elasticity is a good approximation to describe the stress-strain relation (e.g., Tesauro et al., 2012). Thus, for simplicity the three key model parameters in our study are density (ρ), the Young's modulus (E) and the Poisson's

110 ratio (ν). Additionally, the Mohr-Coulomb criteria, using the friction (μ) and the cohesion (C), will be used for some models. As we introduce a fault in our model with different techniques, we solve the problem numerically using the FEM.

2.3 Geometry and material properties

The reference model has an extent of 10 km in each horizontal and 3 km in vertical direction (Fig. 3). The model is intersected in its entirety in the centre by a 60° inclined fault, represented by cohesionless contact elements with a friction coefficient of $\mu = 0.4$ (friction angle $\phi = 21.8^\circ$). The main shortening direction is perpendicular to the strike of the fault.

115 Homogeneous linear elastic and isotropic material properties are assigned to the reference model, having a Young's modulus of $E = 15$ GPa, a Poisson's ratio of $\nu = 0.27$ and a density of $\rho = 2550$ kg m⁻³. The FE-mesh for the reference model has a resolution of 50 m in the X- and Z-direction, and 500 m in the Y-direction. The mesh was created with HyperMesh 2017 and 2019 respectively; the used solver is Abaqus 6.14.1.



The model extend $(10 \times 10 \times 3 \text{ km}^3)$.

Figure 4. Virtual vertical well path in green) with the fault (blue plane) centre of the reference model. Shown are the resulting stress components, inclined by 60° (dip angle) which are S_{Hmax} , in red S_{hmin} , S_V and the visualisation path von Mises stress. The fault with a friction coefficient of $\mu = 0.4$ is traversed at a depth of 660-660 m along which the stress magnitudes are shown. The blue vertical line indicates It is visible that when crossing the location of a vertical well (Fig. 4). The displacement boundary conditions in purple are 10 m shortening ($\epsilon = -1 * 10^{-3}$) in X-direction (perpendicular to the strike direction of the fault), which then governs from the S_{Hmax} magnitude; and 2 m of dilation ($\epsilon = 2 * 10^{-4}$) in Y-direction (parallel hanging wall to the strike direction footwall block, there is a sudden increase of the fault) S_V , which then drives the S_{hmin} magnitude for S_{Hmax} and S_{hmin} a little less.

120 2.4 Model scenarios

The scope of the study is on various factors, which probably contribute to different effects on to investigate factors that affect the stress state in the broader vicinity of faults. These include the element resolution (pre-tests), the representation of the fault

by contact elements with a variable friction coefficient, representation of the fault by elastic weaker elements, or by elements with elasto-plastic rheology, the inclination of the fault, the strike direction relative to the shortening direction, the variation of the rock stiffness (Young's modulus) and the size of the fault and model itself. In order to allow a good readability of the study, specific variations of the model are always briefly explained before presenting the modelling results.

2.5 Initial stress state and boundary conditions

We implement an initial stress state of the model that is in equilibrium with the gravitational forces without resulting in any significant displacement along the fault and the model geometry. We follow the technical procedure as explained in Hergert et al. (2015). In a second step we apply along the model lateral boundaries displacement boundary conditions that result in tectonic stresses throughout the model volume. The main shortening of the reference model is perpendicular to the fault (X-direction) in the order of -10 m ($\epsilon = 1 * 10^{-3}$), which then corresponds to the S_{Hmax} - S_{Hmax} orientation. Parallel to the fault strike (Y-direction), the model undergoes a slight dilation of 2 m ($\epsilon = 2 * 10^{-4}$), which is then the orientation of S_{hmin} - S_{hmin} (Fig. 3). The stress magnitudes resulting from the boundary conditions are shown in Fig. 4 along a vertical synthetic well path in the centre of the model. This stress state is in general agreement with stress magnitude data that were derived from a measurement campaign in Northern Switzerland using >150 Mini-Hydraulic Fracturing and Sleeve Re-Opening test micro-hydraulic fracturing and sleeve reopening tests (Desroches et al., 2021).

~~Virtual vertical well path in the centre of the reference model. Shown are the resulting stress components, which are S_{Hmax} , S_{hmin} , S_V and the von Mises stress. The fault with a friction coefficient of $\mu = 0.4$ is traversed at a depth of -660 m. It is visible that when crossing the fault from the hanging wall to the footwall block, there is a sudden increase of S_{Hmax} and S_V , but S_{hmin} is only little effected.~~

2.6 Stress definition and visualisation

The 3-D stress state of the Earth's crust is described ~~with by~~ a second rank tensor (σ , Jaeger et al., 2011) with nine components, but due to its symmetry only six components are independent from each other. As common in geoscience, compressive stress magnitudes are positive and tensile stresses are negative. The stress state can also be described with the magnitudes and orientations of the three principal stresses. These principal stresses are named from the largest to the smallest as $\sigma_1 > \sigma_2 > \sigma_3$. ~~As common in geoscience, compressive stress magnitudes are positive and tensile stress is negative. $\sigma_1 > \sigma_2 > \sigma_3$.~~

~~Here, we use the differential stress (σ_D) and it's 3-D equivalent, the von Mises stress (σ_{vM} ; Mises, 1913) to visualise the stress state (Eqs. 2 and 3).~~

150
$$\sigma_D = \sigma_1 - \sigma_3$$

$$\sigma_{vM} = \sqrt{\frac{1}{2}(\sigma_1 - \sigma_2)^2 + (\sigma_2 - \sigma_3)^2 + (\sigma_3 - \sigma_1)^2}$$

Furthermore, it is assumed that ~~Furthermore, in our model~~ the vertical stress (S_V) is a principal stress (Eq. 1). ~~The~~ As a result, the two other principal stresses are in the horizontal plane and are labelled as the minimum and maximum horizontal stresses (S_{hmin} and S_{Hmax}).

$$155 \quad S_V = \int_0^z \rho g z, \quad (1)$$

The relative ratio of these three principal stresses defines the stress regime (Anderson, 1905, 1951):

Normal faulting stress regime	NF	$S_V > S_{Hmax} > S_{hmin}$	$S_V > S_{Hmax} > S_{hmin}$
Strike-slip <u>strike-slip</u> stress regime	SS	$S_{Hmax} > S_V > S_{hmin}$	$S_{Hmax} > S_V > S_{hmin}$
Thrust faulting stress regime	TF	$S_{Hmax} > S_{hmin} > S_V$	$S_{Hmax} > S_{hmin} > S_V$

Additionally, we use the differential stress (σ_D) and it's 3-D-equivalent, the von Mises stress (σ_{vM} ; Mises, 1913) to visualise the stress state (Eqs. 2 and 3).

$$\sigma_D = \sigma_1 - \sigma_3 \quad (2)$$

$$160 \quad \sigma_{vM} = \sqrt{\frac{1}{2}(\sigma_1 - \sigma_2)^2 + (\sigma_2 - \sigma_3)^2 + (\sigma_3 - \sigma_1)^2} \quad (3)$$

The model results are presented here in the same way whenever possible. ~~Both the reduced stress tensor, the stresses components S_{Hmax} , S_{hmin} , S_V and the von Mises stress are used to visualise the influence of a fault on the stress state. The results of the models are plotted along a horizontal path at a depth of -660 m (Figs. 3 and 5) for the reference model.~~ This path is always parallel to the main shortening direction (X) and, expect for the models with a variable fault strike. The visualisation
 165 extends from the footwall block at ~~-3.000~~ -3000 m through the fault at 0 m to ~~+3.000~~ +3000 m in the hanging wall block.

2.7 Pre-test: Mesh resolution

The impact of the mesh resolution and sufficiency ~~was~~ is investigated by varying the mesh size, using elastic material properties only, like the reference model. An ~~all-sided resolution of 1.000~~ mesh resolution of 1000, 500, 250 and 100 m in all directions is tested; a finer resolution has been used with an element size of 50 m in the main shortening and depth direction (X and Z), for
 170 which the resolution parallel to the fault (Y) is 500 m.

The model with the coarsest resolution (~~1.000~~ 1000 m) provides stress magnitudes that deviate significantly from the other models (red line in Fig. 6). Even for the model with a resolution of 500 m (magenta line in Fig. 6), the deviation from the higher-resolution models, at a distance greater than ~~1.000~~ 1000 m is clearly visible. All finer-resolution models (≤ 250 m), have

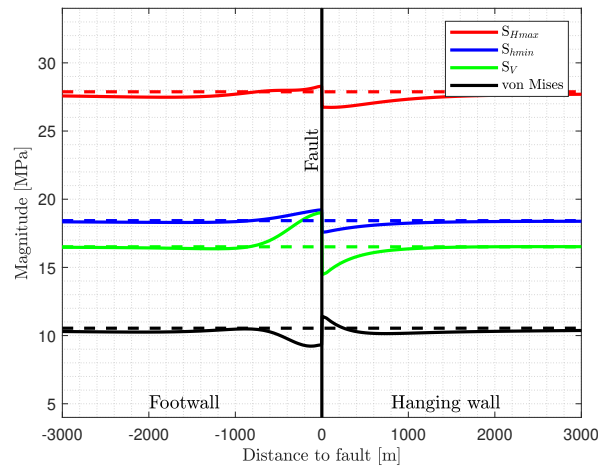


Figure 5. Stress magnitude visualisation of the reference model from -3.000 -3000 m (footwall $-$ left) to $+3.000$ $+3000$ m (hanging wall $-$ right) for a constant depth of -660 m. Used are linear elastic material properties and a friction coefficient of $\mu = 0.4$ for the fault at 0 m, represented by the black vertical line. The dashed lines represent in comparison results of an similar model without a fault.

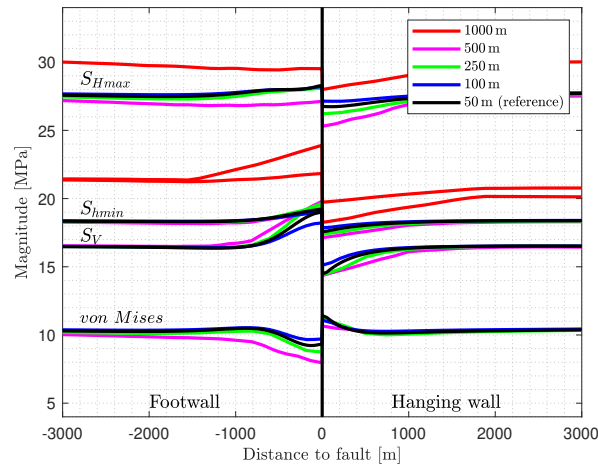


Figure 6. The impact of the mesh resolution is compared. The coefficient of friction of the fault is $\mu = 0.4$ for all models. The coarse resolution models, with $+1.000$ 1000 m (red) as well as 500 m (magenta) show significant deviations from the reference model with a resolution of 50 m (black), while the models with a resolution of 100 m and 250 m (green and blue) show only slight deviations close to the fault.

only small differences close to the fault ($<+1.000$ 1000 m; Fig. 6). This shows, that all models with a resolution of 250 m and finer have a sufficient mesh resolution. A finer mesh is only useful if the magnitude-stress changes close to the fault is of interest, which is not the case in this study.

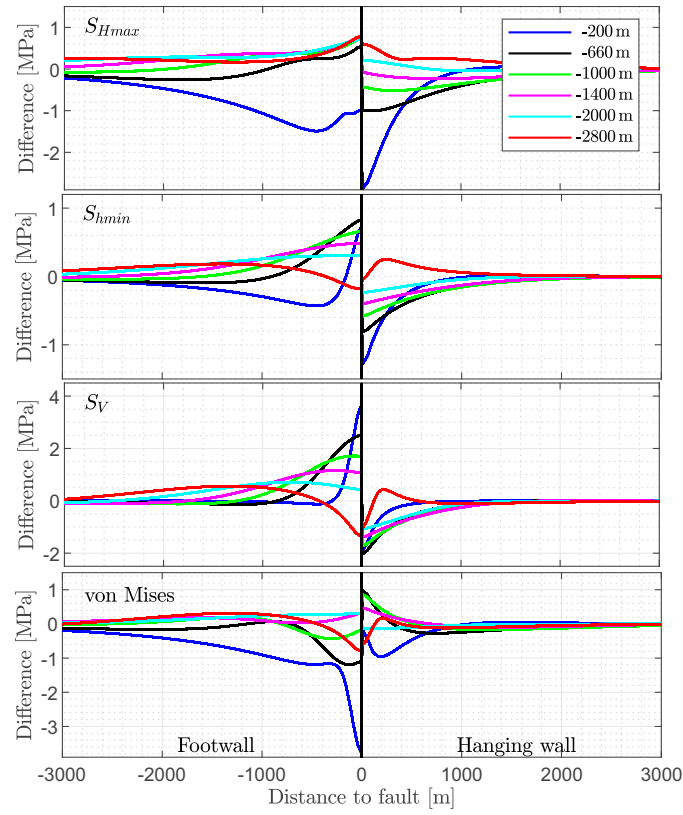


Figure 7. Variation of the stress components (S_{Hmax} , S_{hmin} , S_v and von Mises stress) at different depth levels are shown with respect to the distance of the fault. Stress magnitude changes are visualised along a vertical line at depths of -200 , -660 (reference depth, used by the other figures), -1000 , -1400 , -1400 , -2000 and -2800 m.

3 Results

3.1 Reference model

Within the reference model, the fault is represented by a contact surface ($\mu = 0.4$, $C = 0$). As a result, the components of the reduced stress tensor increase in the footwall close to the fault and decrease in the hanging wall (Fig. 5). S_v and S_{hmin} rise to a similar level (+3 MPa and +1 MPa) within the footwall block near the fault. An opposite behaviour is observed for the von Mises stress. S_{Hmax} , however, increases only slightly close to the fault (<1 MPa); which is the reason for the decrease of the von Mises stress near the fault. Corresponding to these changes, the stress magnitudes decrease next to the fault within the hanging wall block, the largest amount is for S_v , resulting in a slight increase of the von Mises stress. Significant stress changes of more than 1 MPa occur within less than 1000 m away from the fault. The S_{Hmax} orientation is not affected by the fault.

The results of all other models presented subsequently are displayed on a horizontal path at the same depth. For the reference model, the stress variation around the fault for different depth ranges are also shown in Fig. 7. It remains unchanged that stress variations >1 MPa are limited to a distance of about 1000 m from the fault. Relatively large variations can be seen at shallow depths (blue, -200 m) in contrast to greater depths (red, -2800 m). The general patterns of stress variation are similar, except for the vertical stress component. S_V is smaller in the footwall block close to the fault, and larger in the hanging wall block at a depth of -2800 m, in contrast to observation at shallower depth (<2000 m). The reason is that S_V becomes σ_1 (normal faulting regime) for a depth greater than 2000 m, while at shallower depths a transition from a thrust faulting to a strike-slip regime occurs (Fig. 4).

3.2 Friction coefficient

In geomechanics and seismology faults are usually parameterised using the friction coefficient and the cohesion (e.g. Morris et al., 1996; Di Toro et al., 2011). Commonly, a friction coefficient between 0.6 and 0.85 is assumed (Byerlee, 1978) but examples exist of significantly smaller friction coefficients (Di Toro et al., 2011). However, to investigate the influence of the frictional properties of a fault based on the reference model, the friction coefficient is varied from very low ($\mu = 0.1$) to very large ($\mu > 1$). Due to technical limitations cohesion will be always zero.

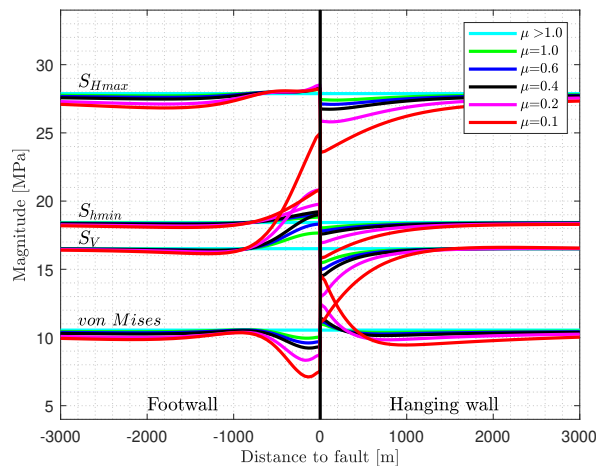


Figure 8. Impact of a variable friction coefficient on the stress state. Plotted are the S_{Hmax} , S_{hmin} and S_V as well as the von Mises stress. The graph with the friction angle of $\mu = 0.4$ is the reference model (Fig. 5). Large stress variations near the fault are a result from low friction.

Using a very large friction coefficient ($\mu > 1$), there is no visible influence by the fault on the stress magnitudes (Fig. 8), the stress magnitudes are identical to a continuous mesh without a contact surface (dashed line in Fig. 5). In contrast, for a low friction case ($\mu = 0.1$), stress variation is significant near the fault. The general pattern is similar as for the reference model, but the increase (footwall: $+8$ MPa) and decrease (hanging wall: -5 MPa) of S_V is much larger. Similar, but not that

205 large stress changes are to observe for S_{Hmin} , $+S_{Hmin}$ changes of $+2$ MPa are observed for the footwall and -2 MPa for the hanging wall block. The drop of S_{Hmax} , S_{Hmax} in the hanging wall block is significant (-4 MPa), whereas the increase in the footwall block next to the fault is negligible. However, a S_{Hmax} , S_{Hmax} decrease of about -1 MPa is visible in both, the footwall- and hanging wall block, even between 1.000 to 3.000 1000 to 3000 m away from the fault. This is a result of stress dissipation due to larger fault offset in the case of low friction. Variation of the von Mises stress is mainly driven by the

210 variation of S_V , S_V . It is mostly σ_3 , trimmed by the fact, that S_V , S_V becomes significant larger then S_{Hmin} , S_{Hmin} in the footwall block about 500 m away from next to the fault for the models with low friction contact definition.

Overall comparison of the models with a different friction in Fig. 8 show, that the stress perturbations gradually decrease with an increase of the friction coefficient. A stress variation of > 1 MPa is limited to a distance of ≈ 1 km, except for S_{Hmax} , S_{Hmax} in the hanging wall block. None of the variation result in a visible change of the S_{Hmax} , S_{Hmax} orientation, it is

215 always parallel to the maximum displacement (X-direction).

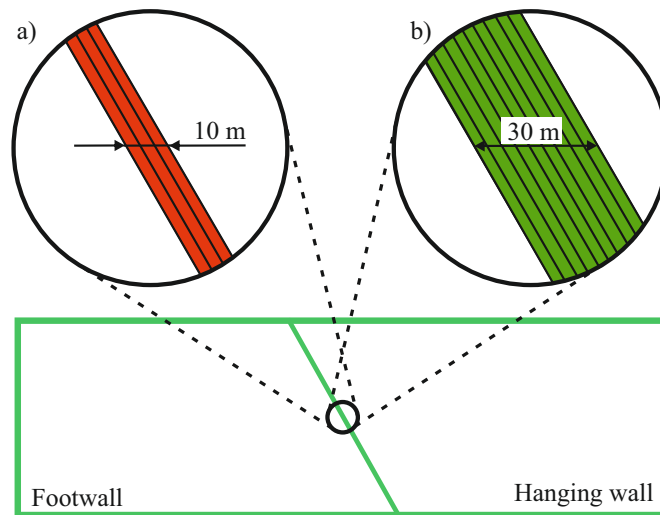


Figure 9. Sketch visualising the representation of the fault zone by elastically weak 3-D-elements with a thickness of a) 10 m made from three elements or b) 30 m made of nine elements. The elements outside this area fault zone are not visualised.

3.3 3-D-fault representation by elastic weak elements

The representation of a fault by a 2-D plane is not realistic for the immediate vicinity of the fault where a zone of damaged rock is expected. A more realistic approach seems to be the representation by a 10 m thick layer of elements with elasto-plastic rheology an elastic rheology of reduced stiffness (Fig. 9-a). This simulates the reduced stiffness due to the damage zone in and

220 damage zone around the fault core (e.g., Faulkner et al., 2006). The three element thick layer has a

Herein, the fault zone has a width of 10 m represented by three elements normal to the fault (Fig. 9 a). A Young's modulus of $E = 5, 1$ and $0.1250, 25$ GPa, in contrast to is tested while the stiffer surrounding having has $E = 15$ GPa. The element resolution outside the fault area is 50 m in X- and Z-direction and 500 m in the Y-direction.

The stress magnitudes along the profile (Fig. 10) do not show a significant stress variability in the vicinity of the fault resulting from three the less stiff elements. Stress changes are restricted to the a very narrow domain, which are not visible; they are visually hidden behind the fault line. S_{Hmax} S_{Hmax} decreases depending on the decreasing stiffness. For the model with $E = 250$ MPa fault representation, S_{Hmax} S_{Hmax} is always around 1 MPa lower because of stress dissipation by the low stiff fault domain. Therefore, the von Mises stress drops by the same amount. Stress dissipation also effects S_{hmin} S_{hmin} , but with a much lower amount; for S_V S_V no effect is visible.

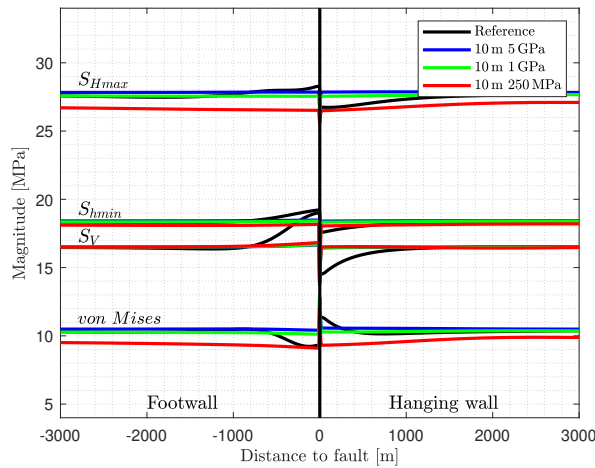


Figure 10. Fault representation by a 10 m thin layer of three weak elements. The fault elements have a lower Young's modulus ($E = 5, 1$ and $0.1250, 25$ GPa) in contrast to the area outside this region ($E = 15$ GPa). Shown in black is the reference model, and vertically the implemented fault zone. Stress changes are narrowly limited to the area of the fault so that they are hidden by the visualisation of the fault zone.

Another model version has a thicker fault representation by of 30 m, made from nine elements represented by nine elements normal to the fault (Fig. 9 b). Like the 10 m models, S_{Hmax} S_{Hmax} drops especially for the model with the least stiff fault domain ($E = 250$ MPa) by around -3 MPa (Fig. 11), again an effect of the stress dissipation. S_{hmin} S_{hmin} decreases by almost 1 MPa, whereas S_V S_V is stable. Near the fault, S_{Hmax} , S_{hmin} and S_V decreases S_{Hmax} , S_{hmin} and S_V decrease significant, limited to a region, narrow to the fault (< 100 m). The von Mises stress variation is mainly driven by the reduction of S_{Hmax} S_{Hmax} because of the less stiff fault parts. There is no change of the S_{Hmax} S_{Hmax} orientation to observe ; it is stable and it remains parallel to the X-direction.

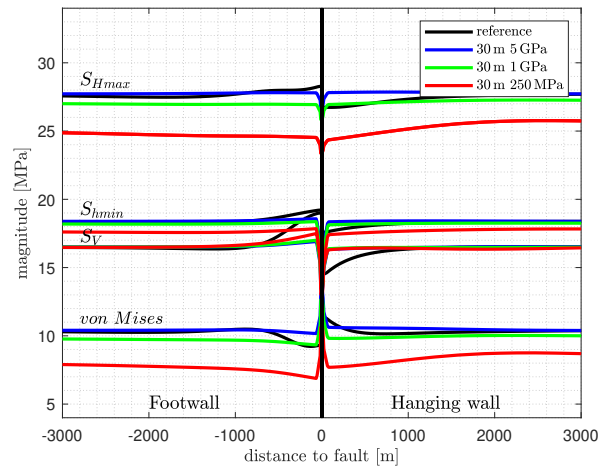


Figure 11. Fault representation by 30 m (nine elements) of elastic weak elements having a lower Young's modulus ($E=5, 1$ and $0.1, 250, 250$ GPa), compared to the area outside this region with $E=15$ GPa. In colours are the model results with the less stiff 3-D-fault representation. Shown in black is the reference model using contact surfaces, in colours are and vertically the model results with the less stiff 3-D-fault representation implemented fault zone at 0 m.

3.4 3-D-fault representation by elements with elasto-plastic rheology

As purely elastic elements do not allow failure, they cannot dissipate stresses such as a contact surface is able to do. To accommodate both, the ability to dissipate stresses and the representation of a damage zone, elements with elasto-plastic rheology within the fault zone are now used. Out of a continuous mesh, elements close to the fault location were selected in a staircase-like manner, which have a specific plastic yield criterion. These fault elements have laterally a range of one (Fig. 12 a) to eight elements (Fig. 12 b). These elements have a friction angle of $\phi = 30^\circ$ (friction coefficient $\mu = 0.58$) and a low cohesion of $C = 0.1$ kPa. The used dilatation-dilation angle is $\psi = 25^\circ$. In contrast to that, the non-fault elements have a much larger cohesion ($C = 500$ kPa), but the same friction- and dilation angle. The element resolution in the vicinity of the fault is 100 m in X- and Z-direction, and 500 m in the Y-direction. The elastic material properties are the same as used by the reference model ($E = 15$ GPa, $\nu = 0.27$ and $\rho = 2550$ kg m⁻³).

The representation by means of staircase-like elements with elasto-plastic properties (Fig. 13) shows that the impact on the stress components is nearly independent from the amount of laterally used elements that allow plastification. S_{Hmax}, S_{hmin}, S_V rises a little bit S_{Hmax}, S_{hmin}, S_V slightly increase in the footwall block near the fault domain and is a little bit lower slightly decrease in the hanging wall block, again near the fault domain. The overall variation of $S_{Hmax}, S_{hmin}, S_V, S_{Hmax}, S_{hmin}, S_V$ and the von Mises is < 1 MPa. Stress magnitudes do not show any discontinuous behaviour at the fault zone, as the reference model do. Stress variations are restricted to a zone less than 1.500 of about 1000 m next to the fault domain. Again, the $S_{Hmax} S_{Hmax}$ orientation is not disturbed as a result of the fault.

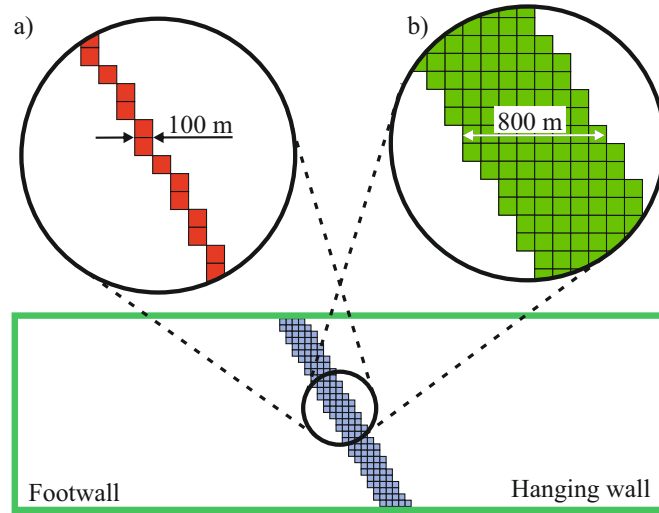


Figure 12. Sketch showing the fault representation by selected elements out of the mesh, which plastify as a result of friction and a low cohesion of $C = 0.1$ kPa. Elements outside this region (white area, mesh not shown) have a cohesion of $C = 500$ kPa, the white area, where the mesh is not shown. A friction angle $\phi = 30^\circ$ (friction coefficient $\mu = 0.58$) is used for all elements for the first test. Different number of lateral elements, representing the fault are tested, ranging from one (a) to eight (b) lateral elements. As the element size is 100 m near the fault, the total width of the stair-step like fault ranges from 100 to 800 m.

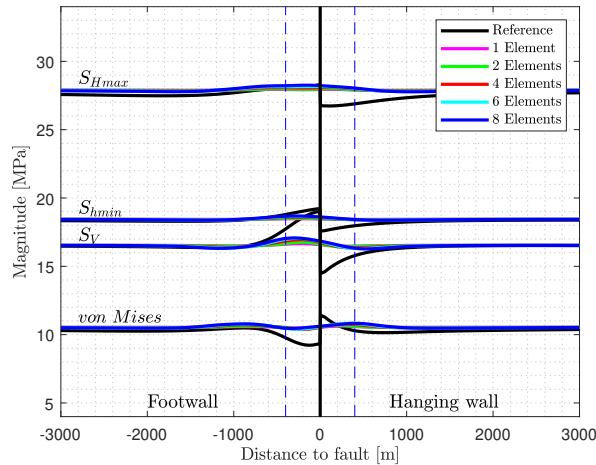


Figure 13. Fault representation with staircase-like elements with elasto-plastic rheology (Fig. 12) that are allowed to deform non-elastically. Shown in black is the reference model with the implemented fault, in colours are the models with a continuous mesh with the one (magenta) to eight lateral elements (dark blue). These elements have a low cohesion of $C = 0.1$ kPa and a friction angle of $\phi = 30^\circ$ (friction coefficient $\mu = 0.58$). The maximum width of eight elements is visualised by the dashed blue lines.

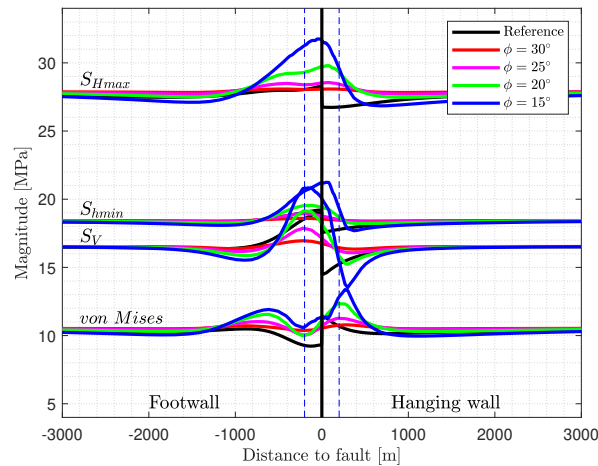


Figure 14. Fault representation with four staircase-like elements with elasto-plastic rheology (Fig. 12) that are allowed to deform non-elastically. Shown in black is the reference model and the fault centre (vertical), in colours are the models with a friction angle of $\phi = 30, 25, 20$ and 15° . The $\phi = 30^\circ$ model is the same as the four element model in Figure 13. The width of four elements is visualised by the blue dashed lines.

The model having laterally four weak elements is used again to investigate the impact of the friction angle (ϕ). Fig. 14 shows the result, where a friction angle of $\phi = 30, 25, 20$ and 15° is applied. The $\phi = 30^\circ$ model has already been used for the variation of the number of lateral elements (Fig. 13: 4 Elements). Modelling results in Fig. 14 show, that a decreasing friction angle increases the stress variation near the fault. S_{Hmax}, S_{Hmin}, S_V rises S_{Hmax}, S_{Hmin}, S_V increase in the footwall block near the fault, where while a slight decrease can be seen in the hanging wall block. However, swing-in effects can be observed on both sides of the fault. Largest magnitude changes are about +4.5 MPa for S_V , +5 MPa for S_{Hmax} and +2.5 MPa for S_{Hmin} . In a distance of >1400 m, to the fault centre, the variation of the stresses is <1 MPa. The S_{Hmax} orientation keeps S_{Hmax} orientation remains unaffected.

Fault representation with four staircase-like elements with elasto-plastic rheology (Fig. 12) that are allowed to deform non-elastic. Shown in black is the reference model and the implemented fault (vertical), in colours are the models with a friction angle of $\phi = 30, 25, 20$ and 15° . The $\phi = 30^\circ$ model is the same as the four Element model in Figure 13. The width of four elements is visualised by the blue dashed lines.

3.5 Variation of the fault dip angle

To study the impact of the fault dip angle, several models with different fault inclination are prepared. These models have an dip angle of $30^\circ, 40^\circ, 50^\circ, 70^\circ$ and 80° , in contrast to the reference model (60° , Fig. 3 and 5). Elastic material properties are the same as used by in the reference model: $E = 15$ GPa, $\nu = 0.27$, $\rho = 2550$ kg m $^{-3}$ and fault representation by contact elements: $\mu = 0.4$ and $C = 0$.

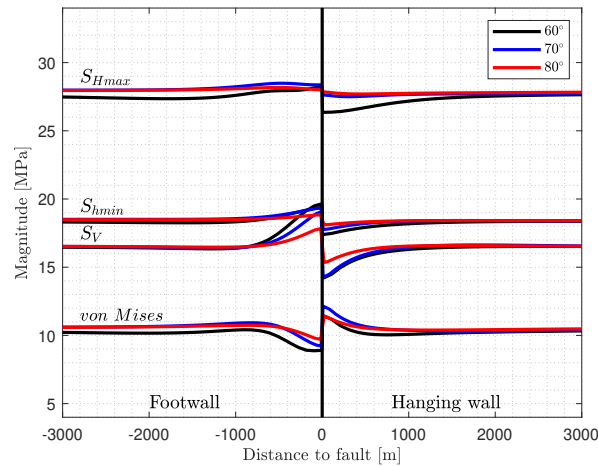


Figure 15. Influence of the dip angle of the fault on the stress components S_V , S_H , S_{Hmax} , S_{Hmin} and the von Mises stress. Shown are the models with a fault dip angle of 60° (reference model), 70° and 80° . By increasing the dip angle, the magnitude of stress perturbation decreases.

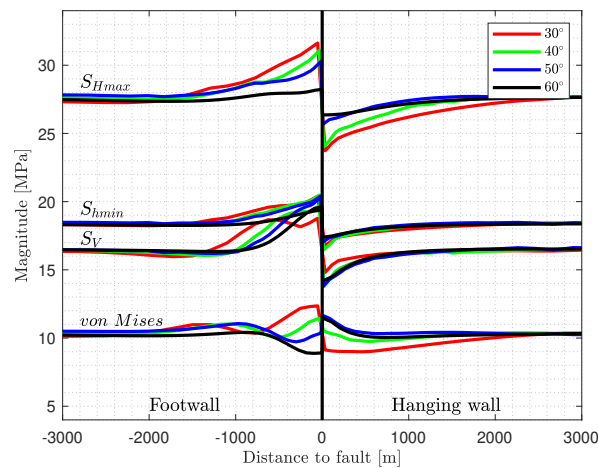


Figure 16. Influence of the fault dip angle on the stress components. A range of fault dip angles are presented, including 60° (reference model), 50° , 40° and 30° of the fault dip angle is shown. By reducing the dip angle, the stress magnitude change changes and the distance of the lateral stress perturbation increases. The most pronounced stress perturbation is seen for shallow dipping faults (30° in red).

In Fig. 15, it can be seen that the stress perturbation pattern is similar compared to the reference model. With increasing dip angle from 60° (reference model) to 70° and 80° , the stress perturbation slightly decreases. The reduction is most signifi-

cantly visible for the S_V - S_V magnitude in the footwall block next to the fault. Stress magnitudes away-in-a-distance from the fault increase slightly for the large dip angle models, as the stress dissipation by the fault decreases.

275 A decrease in dip angle of the fault results in a significantly more pronounced increase of the stress perturbation near the fault (Fig. 16). This leads-to-results-in an increase of S_{Hmax} - S_{Hmax} by >4 MPa in the footwall block, and a decrease of about ~~-4-4~~ MPa in the hanging wall block, using an fault inclination of 30°. There-is-also-a-clear An-increase-of-the- S_V and S_{Hmin} magnitudes in the footwall block and a decrease in the hanging wall block is clearly visible. The influence of the fault on the ~~S_{Hmax} - S_{Hmax}~~ magnitude on both, the footwall and hanging wall block, ~~is~~ in a distance to the fault of about ~~1.500~~1500 m and
280 ~~2.000~~2000 m. An-increase-of-the- S_V and S_{Hmin} magnitudes in the footwall block and a decrease in the hanging wall block is clearly visible However, the large distance is an effect of the small fault dip, the real distance is half of that values for the 30° model. There is no perturbation of the S_{Hmax} - S_{Hmax} orientation.

3.6 Variation fault strike angle

In addition to the influence of the dip, the influence of the S_{Hmax} - S_{Hmax} orientation with respect to ~~that-of~~ the fault strike is
285 investigated. Thus, an strike angle of 90° as the reference model is compared with other models where the fault is striking with an angle of ~~70, 75, 60, 45, 30 and 15°~~. In-order-to-allow-geometrically To-geometrically-allow such strike angles, the models are extended in the X-direction from 10 km to 20, 30 and 50 km for the models-with-an-fault-strike-of-45°, 30° and 15° models, respectively- respectively. The resulting boundary conditions are adapted, to-allow-adjusted, to-ensure comparability.

Results of the strike angle variation (Fig. 17) are shown ~~parallel-to-the-shortening-direction- S_{Hmax} and not~~ perpendicular to the strike direction of the fault. The impact of the fault strike variation on the ~~S_{Hmax} and S_{Hmin}~~ S_{Hmax} and S_{Hmin} magnitude is minimal. Clear deviations ~~to-the-reference-model-are-only-for- S_V are only observed for S_V~~ in the footwall block. ~~However, next to the fault, S_V is smaller for these models as,~~ where S_V is smaller compared to the reference model. ~~For the 15, 30 and 45~~ As a result, the von Mises stress is also less variable in the footwall block, next to the fault The variation of the S_{Hmax} orientation varies with distance to the fault, but does not exceed 1.5° ~~strike-model, the S_V magnitude is significant larger up to 2.500 m~~
295 ~~away from the fault. But this distance is parallel to the main shortening direction. The distance normal to the contact is about 650 m-,~~ which is significantly smaller than the uncertainties of orientation data records (Heidbach et al., 2018). Therefore, no visualisation of that is shown.

~~As the fault strike is not perpendicular to the maximum compression for the horizontal stress orientation, deviation of S_{Hmax} occur from-~~

300 Since the models with the fault strike variation and the friction coefficient of 0.4 only cause small S_{Hmax} rotations, the influence of a lower friction ($\mu = 0.1$) is also investigated. The plot of the stress magnitudes (Fig. 18) shows a visible variation of the magnitudes for the different orientations of the fault. The general pattern is similar to the reference model. For S_{Hmax} , significant variations in stress magnitude are observed between the models due to stress dissipation resulting from low friction at the fault. The largest magnitudes are for the ~~orientation-of-the~~ reference model (90°) as well as the 15° model. In contrast,
305 the 45°, where S_{Hmax} is always 030° ~~-.The angular- and 60° models have the largest S_{Hmin} magnitudes.~~ As a result of the largest

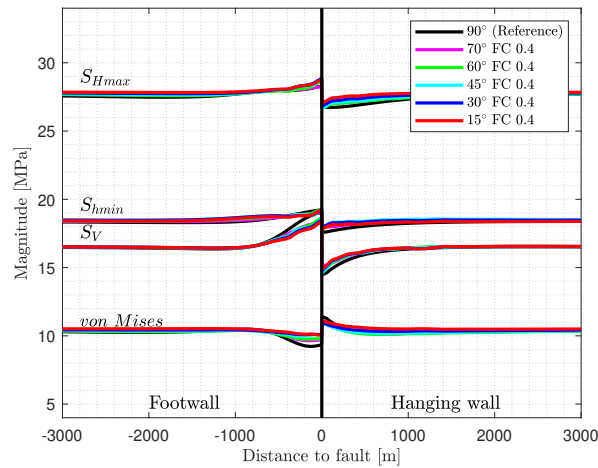


Figure 17. Variation Stress components are shown for the models with a variation of the strike angle, relative to the orientation of the maximum shortening using a friction coefficient of $\mu = 0.4$. In contrast to the reference model with a fault strike angle of 90° , the varied models have a strike angle of 70° , 60° , 45° , 30° and 15° . The stress components are plotted parallel to the shortening direction and not perpendicular to the strike of the fault.

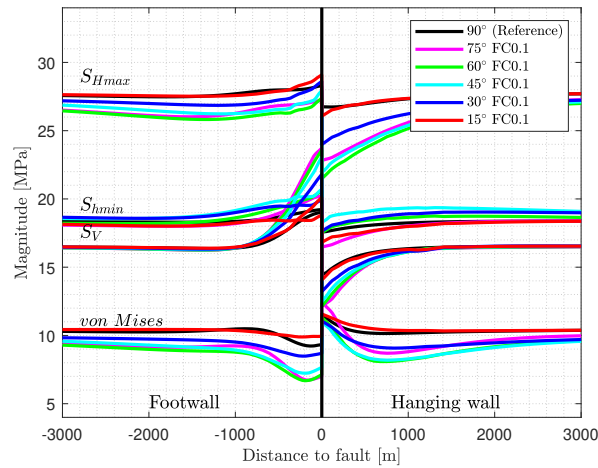


Figure 18. Variation of the strike angle, with 90° (reference), 75° , 60° , 45° , 30° and 15° relative to the orientation of the direction of maximum shortening. Used is a friction coefficient of $\mu = 0.1$ in contrast to the similar models with a friction coefficient of $\mu = 0.4$ (Fig. 17). The stress components are plotted perpendicular to the strike of the fault.

variation of the S_{Hmax} orientation varies with distance to the fault, but does not exceed $1.5 S_{Hmax}$ magnitudes, the lowest von Mises stresses are observed for 45° , 30° and 60° models.

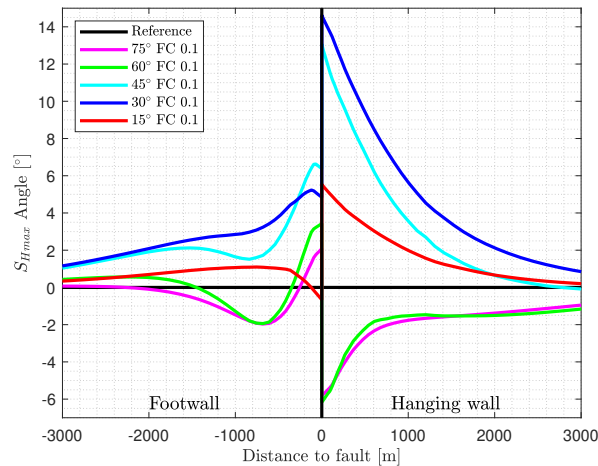


Figure 19. Variation of the strike angle (75° , 60° , 45° , 30° and 15°), relative to the orientation of the maximum shortening direction using a friction coefficient of 0.1. Shown are the variation of the S_{Hmax} orientation, compared to the reference model with a fault strike angle of 90° and an constant S_{Hmax} orientation of 0° . The angular variation is plotted perpendicular to the strike of the fault.

For the first time in the model series, a significant variation in the orientation of S_{Hmax} is clearly visible with a fault strike variation using a friction coefficient of $\mu = 0.1$ (Fig. 19). This value should be taken with caution in the near-field (<100 m) to the fault. The deviation of the orientation reaches up to about 14° in the hanging wall block for the model with an fault strike of 30° , closely followed by the 45° model. The S_{Hmax} rotation for the 30° , as the element resolution is not chosen to investigate the stress pattern next to 45° and 15° models is clockwise, parallel to the fault strike of the fault, while in the models with a strike of the fault of 60° as well as 75° , S_{Hmax} orientation is counterclockwise, i.e. tends to be perpendicular to the orientation of the fault. In the footwall block, the rotation of S_{Hmax} is also visible, but less than in the hanging wall block, with maximum of about 6° .

3.7 Young's Modulus

Since the elastic material properties have a significant influence on the deformation of on the rock of both sides of the fault, the Young's modulus was of the host rock is varied. In addition to the Young's modulus of the reference model ($E = 15$ GPa), stiffnesses of 5, 20, 30, 40, 60, 80 and 100 GPa are tested. In order to make keep the model comparable, the boundary conditions are adopted-adapted (Tab. 2), so that the far-field stress magnitudes of the different models were equal.

The variation of the Young's modulus has limited effect on S_{Hmax} in the footwall block (Fig. 20), where in the hanging wall block S_{Hmax} decreases S_{Hmax} decreases by up to -4 MPa with increasing Young's modulus next to the fault. S_{hmin} S_{hmin} increases slightly with the Young's modulus in the footwall block, and decreases in the same way in the hanging wall block slightly, by up to -2 MPa. The S_V S_V magnitude shows the same pattern, but the stress deviation is much larger near the

Table 2. Boundary conditions are chosen depending on the Young’s modulus to generate equal far-field stress magnitudes for the different models. The boundary conditions for 15 GPa are the reference model settings.

Young’s Modulus [GPa]	X-shortening [m]	Y-dilation [m]
5	30.000	6.000
15	10.000	2.000
20	7.500	1,500 1,500
30	5.000	1.000
40	3.750	0.750
60	2.500	0.500
80	1.875	0.375
100	1.500	0.300

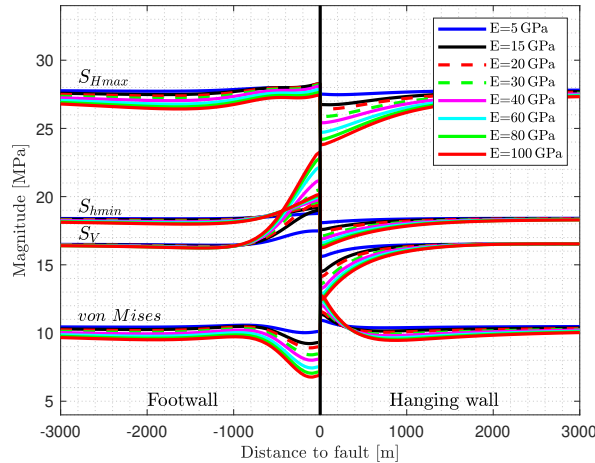


Figure 20. The influence of the Young’s modulus on the stress perturbation is investigated. The models have a Young’s modulus of $E = 5, 15$ (reference model), 20, 30, 40, 60, 80 and 100 GPa.

325 fault, up to +7 MPa in the footwall and -4.5 MPa in the hanging wall block. The von Mises stresses decrease with increasing
 Young’s modulus in the footwall block next to the fault and increases in the hanging wall block next to the fault.

In general, the stress perturbation increases due to a larger Young’s modulus, as stress dissipates on the fault. The lateral
 influence of the fault on the stress components, producing a stress variation of more than 1 MPa, is limited to a range from
 -1.000 1000 m to $+1.000$ 1000 m next to the fault. Again, the S_{Hmax} orientation is always parallel to the direction of

330 principal shortening.

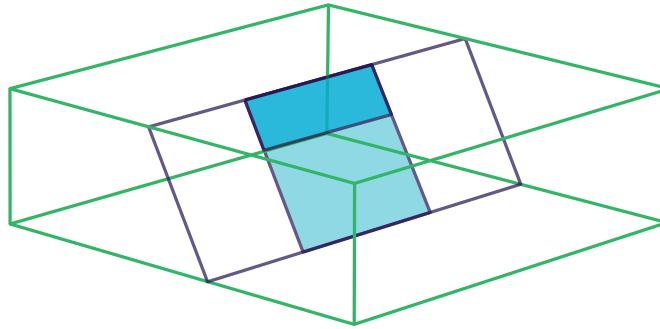


Figure 21. Model sketch with a reduced fault surface area of $4 \times 3 \text{ km}^2$ (light and dark blue areas together) and $4 \times 1 \text{ km}^2$ (dark blue area only). Everything else is just the same as shown by Fig. 3.

3.8 Model size

It is obvious that the influence of the fault on the stress state also depends on the size of the fault surface or on the overall size of the model. For this purpose, the size of the active fault surface using the reference model geometry ~~was reduced to a size of 4.000 km^2~~ is reduced to $4000 \times 1000 \text{ m}^2$ and $4000 \times 3000 \text{ m}^2$ (Fig. 21). Also, the reference model with the full fault surface ~~was also is~~ doubled and quadrupled in size. The resulting models then have dimensions of $20 \times 20 \times 6 \text{ km}^3$ and $40 \times 40 \times 12 \text{ km}^3$, respectively. The resulting mesh resolution ~~was is~~ then 100 m and 200 m in the X- and Z-directions, respectively, and 1 and 2 km in the strike direction (Y) of the fault, which is parallel to S_{hmin} . The boundary condition ~~was were~~ adjusted accordingly, to generate a similar stress state.

~~Influence of the fault size on the stress components. Models with a reduced fault surface area with a size of $4 \times 3 \text{ km}^2$ and $4 \times 1 \text{ km}^2$ (Fig. 21), as well as models like the reference model with a total size of $20 \times 20 \times 6 \text{ km}^3$ (double size) and $40 \times 40 \times 12 \text{ km}^3$ (quadruple size) are shown.~~

The comparison of the results in Fig. 22 shows that as the size of the fault increases, the magnitude deviation near the fault increases. Thus, in the ~~footwall block S_{Hmax} hanging wall block S_{Hmax}~~ is reduced by almost -3 MPa , while ~~S_{V} in the hanging wall S_{V} in the footwall~~ block is increases by more than $+5 \text{ MPa}$ for the model with side length of 40 km. As a result, the von Mises stress in the footwall block decreases more significantly close to the fault. However, the increase of the fault surface area does not have a significant influence on the far-field stress pattern. Significant stress changes ($>1 \text{ MPa}$) occur up to about ~~1.000 m~~ next to the fault. ~~No rotation of the S_{Hmax} orientation can be observed.~~

3.9 Strain variation

The effect of stress anisotropy is studied by defining variable lateral boundary conditions. The shortening, perpendicular to the fault strike (X-direction) is tested from 1, 2, 3, 4, 6, 8, 10 (reference model), 12, 14, 16 and 20 m ($\epsilon = -1 \times 10^{-4}$ to -2×10^{-3}), where the dilation to the fault (Y-direction) remains identical to the reference model of -2 m ($\epsilon = 2 \times 10^{-4}$). Everything else is identical to the reference model.

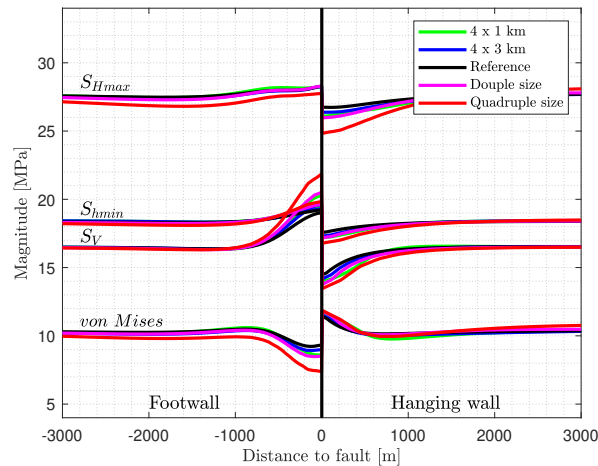


Figure 22. Influence of the fault size on the stress components S_{Hmax} , S_{hmin} , S_V and the von Mises stress. Models with a reduced fault surface area with a size of $4 \times 3 \text{ km}^2$ and $4 \times 1 \text{ km}^2$ (Fig. 21), as well as models like the reference model with a total size of $20 \times 20 \times 6 \text{ km}^3$ (double size) and $40 \times 40 \times 12 \text{ km}^3$ (quadruple size) are shown.

The different S_{Hmax} magnitudes result directly from the variable shortening, applied to the model boundaries (Fig. 23). The overall pattern is like the reference model. The observed variation is low for low strain, where variation is larger for higher strain. S_{Hmax} is smaller than the average S_{Hmax} is smaller for larger strain away from the fault and rises increases a bit next to the fault. In the footwall block, the pattern is clear: the closer to the fault, the smaller is S_{Hmax} .

The variation of S_{hmin} is similar to S_{Hmax} , variation is small for less shortening and rises increases by increasing shortening of the model (Fig. 23). S_{hmin} increases in the footwall block next to the fault and is smaller next to the fault in the hanging wall block.

Larger variation can be seen for S_V , with an increase in the footwall block and a decrease in the hanging wall block. The S_V magnitude variation increases from S_V magnitude variation in the footwall block increases from +0.4 MPa for 2 m of shortening to +2.3 MPa for 20 m of shortening. Nearly the similar amount of decrease happens in the hanging wall block.

The von Mises stress variation (Fig. 23) increases with the rise increase of shortening compared to the reference model. For the model with little strain ($< 4 \text{ m}$) the observed variation of the von Mises stress displays another pattern. For them, the von Mises stress increases in the footwall block and decrease in the hanging wall block, next to the fault. Again, major stress variations are restricted for limited to a distance of less than 1000 m next to the fault. S_{Hmax} The S_{Hmax} orientation is not affected for larger shortening perpendicular to the fault. For the models with a shortening of 1 and 2 m of shortening in the X-direction, under an dilation of 2 m in the Y-direction, there is no clear S_{Hmax} orientation anymore, it becomes chaotic (not shown) the stress magnitudes is horizontally isotropic ($S_{hmin} = S_{Hmax}$) and the S_{Hmax} orientation is not clearly defined.

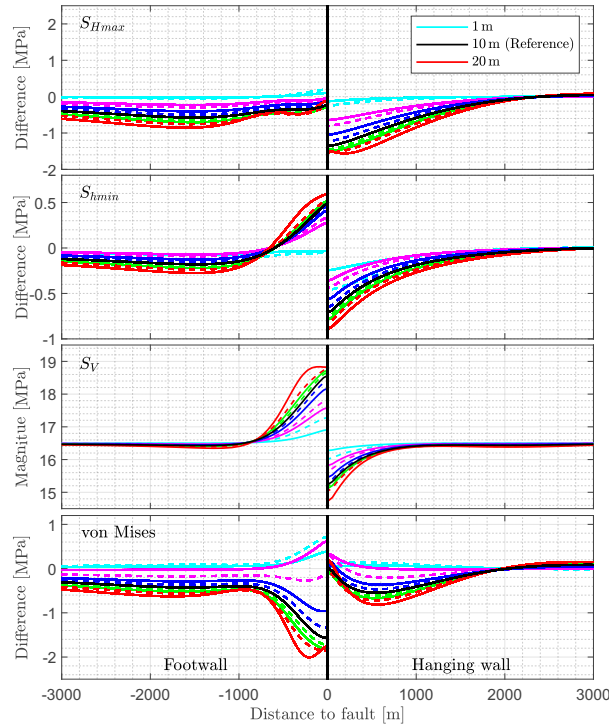


Figure 23. Influence of a variable strain on the stress components are shown. The models have a shortening of 1, 2, 3, 4, 6, 8, 10 (reference), 12, 14, 16 and 20 m ($\epsilon = -1 \cdot 10^{-4}$ to $-2 \cdot 10^{-3}$) perpendicular to the strike of the fault (X-direction) and a constant dilation of 2 m ($\epsilon = 2 \cdot 10^{-4}$) parallel to the fault (Y-direction). Avoiding an overload on the legend, only the 1, 10 and 20 m ~~model-models~~ are indicated there. As the different lateral strain along the model boundaries result in different stress magnitudes, only the relative stress changes (local stresses ~~far field~~ ~~far-field~~ stress) are shown for S_{Hmax} S_{Hmax} , S_{hmin} S_{hmin} and the von Mises stress. The general pattern of stress variation is like the reference model, the variation is smaller for lesser strain and larger for more strain. However, relative variation of the stress components are not bigger as about ± 1.5 MPa for S_{Hmax} S_{Hmax} , S_{hmin} S_{hmin} , around 2 MPa for the von Mises stress and about 2.3 MPa for S_V S_V .

370 4 Discussion

4.1 Model ~~simplification~~ ~~set up and assumptions~~

~~Simple numeric models are generated, where different geometries, technical approaches and different material properties are used to represent a fault or a fault zone.~~ The goal is to investigate the impact of faults on the ~~far field~~ ~~far-field~~ stress state (>100 m). The model design does not allow estimations on the stress state or stress perturbations close to a fault (<100 m).

375 Investigating that, a much finer mesh resolution would be needed. It is also questionable whether and which methods of fault implementation are suitable for this purpose.

Like all generic models, those ones used here are a ~~strong~~ ~~significant~~ simplification of rock physics, geological structures, and the fault representation itself. Except for two scenarios, only linear elastic material properties are used to represent the rock vol-

ume. This neglects various rheological processes within the Earth's crust. But Hooke's law seems to be a proper approximation
380 for the major mechanical behaviour of rocks in the upper crust, as the elastic thickness of the crust (T_e) is usually much larger
than the models used here (Burov and Diament, 1995; Hyndman et al., 2009; Tesauro et al., 2012). According to field investi-
gations by Maerten et al. (2016), most brittle deformation can be explained using linear elastic material properties. Furthermore,
the focus is not on stress changes during the co-seismic phase (e.g., Brodsky et al., 2020; Lin et al., 2013; Shi et al., 2020; Zhang and Ma, 2021
(e.g., Lin et al., 2013; Brodsky et al., 2020; Shi et al., 2020; Zhang and Ma, 2021), or deformation over several seismic cycles.
385 The focus is on the quasi-static stress state in the inter-seismic phase.

The reference geometry is a normal faulting structure with a fault dip of 60° , but the applied boundary conditions result in a thrust- to strike-slip faulting regime at the depth, where stresses are plotted, usually at -660 m. Even if most models use specific structures and specific stress regime conditions, other structural settings or faulting regimes are covered by some of the models or specific result presentations. These are the variation of the dip angle (Fig. 15 and 16), the variation of the strain
390 (Fig. 23) and the variation of the depth for the reference model (Fig. 7). Therefore, results for all stress regimes and faulting structures are provided. However, the overall behaviour remains unchanged.

The specific objective was to investigate how faults can lead to stress rotations since this has been claimed to be the reason for observed stress rotations on scales of 10's of km. However, for most scenarios only stress magnitudes are shown here. This is of course due to the fact that many models do not show S_{Hmax} rotations. Visualising the stress magnitudes gives a much
395 broader insight into the effect of faults on the stress state. And, if the stress magnitudes change, stress rotation is possible, but if the magnitudes do not change, rotation can be ruled out. Therefore, the stress magnitude visualisation used also acts as a proxy for potential stress rotation.

To allow good comparability of modelling results, constant boundary conditions ~~has~~have been used, with a few exceptions. The models with different strain have ~~of course~~ different stress magnitudes as a result. For models having a different ~~extend~~
400 extent or a variable Young's modulus, the boundary conditions were scaled accordingly to ensure comparability. The models with a lower Young's modulus in the fault zone and low friction contact faults dissipate localised stresses, which has not been corrected, as the influence on the result are ~~negligible~~small.

4.2 Discontinuity approach: contact elements

Several of the model scenarios use contact elements to represent a fault within the model. This is the case for the reference
405 model, the variation of the friction, the fault dip- and fault strike angle, the Young's modulus variation in the ~~country~~host rock, the model size and the boundary conditions. The overall observation is an increase of the stress components (~~S_{Hmax} , S_{Hmin} and S_V~~ S_{Hmax} , S_{Hmin} and S_V) in the footwall block and a decrease within the hanging wall block, both next to the fault (Fig. 24 a-d). In contrast, the von Mises stresses decreases in the footwall block and increases in the hanging wall block. This is the case as ~~S_V , which is mostly σ_3~~ S_V varies more than the other stress components.

410 For these contact surfaces ~~we assume~~, no cohesion ($C = 0$) ~~which is a reasonable~~is used, which is nevertheless a reasonable and conservative simplification in particular for pre-existing faults or fault zones, as granular material have a very low cohesion: $C < 1$ kPa (Schellart, 2000). On the other hand, cohesion strengthening can increase the cohesion to $C > 1$ MPa (van den

Ende and Niemeijer, 2019), $C = 8$ MPa (Muhuri et al., 2003) or $C = 35$ MPa for very high temperatures (Tenthorey and Cox, 2006). According to Tenthorey and Cox (2006), cohesion will reach 3 MPa for ~~an 100 years recurrence interval for a~~ 100-year earthquake recurrence interval at a depth of about 2 km.

The used friction ~~coefficient (μ) coefficients~~ for the contact surfaces ~~reaches reach~~ from 0.1 over 0.4 (reference model) to 1.0 and larger. In the past, it was assumed, that the friction coefficient of faults is about 0.6 to 0.85 (~~Byerlee, 1978; Brace and Kohlstedt, 1980; B~~ (Brace and Kohlstedt, 1980; Byerlee, 1978; Brudy et al., 1997)). But the ~~μ -friction~~ can be much smaller, if clay minerals dominate (Byerlee, 1978; Lockner et al., 2011), in the case of dynamic offset (Di Toro et al., 2011; Boulton et al., 2017) or for high pore pressures (Blanpied et al., 1992; Byerlee, 1993).

Low friction is also expected for large fault (zones) or subduction zones (~~Fulton et al., 2013; Bird and Xianghong Kong, 1994; Iaffaldano~~ (Bird and Xianghong Kong, 1994; Carena and Moder, 2009; Iaffaldano, 2012; Fulton et al., 2013; Carpenter et al., 2015; Houston, 2015)). The friction coefficient is in the order of 0.08 for the 2011 Tohoku-Oki Earthquake (Fulton et al., 2013), $\mu = 0.12$ – 0.25 or 0.05 – 0.2 for the San Andreas Fault (Bird and Xianghong Kong, 1994; Carena and Moder, 2009) or for tremors in general $\mu = 0$ to ~~0.1 – 0.1~~ 0.01 – 0.07 (Houston, 2015). Iaffaldano (2012) assumes a friction coefficient of ~~0.01 to 0.07~~ 0.01 to 0.07 for large scale plate boundaries. However, the investigated range of ~~μ -friction~~ cover this variation well, except for $\mu < 0.1$.

As a free surface, or a fault with very low friction coefficient, is unable to build up shear stresses (Hafner, 1951), principal stresses will be parallel and perpendicular to the surface (~~Camac and Hunt, 2009; Bell, 1996; Hudson and Cooling, 1988; Osokina, 1988; P~~ (Hudson and Cooling, 1988; Osokina, 1988; Rawnsley et al., 1992; Petit and Mattauer, 1995; Bell, 1996; Camac and Hunt, 2009)). A classic example is the San Andreas Fault (Mount and Suppe, 1987), where the interpretation of borehole breakouts and drilling induced tensile fractures from near-by borehole indicate in ~~S_{Hmax} – S_{Hmax}~~ orientations that are almost perpendicular to the fault (~~Mount and Suppe, 1992; Zoback et al., 1987~~) (Zoback et al., 1987; Mount and Suppe, 1992). However, the distance of these boreholes is ~~>1.0001000 m~~ from the fault core in most cases and thus it is questionable that the derived ~~S_{Hmax} – S_{Hmax}~~ orientations can be used as an observable for the fault strength. Hickman and Zoback (2004) show in their analysis of borehole breakouts and drilling induces tensile failures of the SAFOD borehole through the San Andreas fault that significant S_{Hmax} rotations can only be resolved in the near field of the fault.

4.3 Continuity approach: Weak elements as fault zone

4.3.1 Young's modulus variation in the fault zone

Fault representation by elastic weak elements exhibits no significant stress variation pattern using three elements (Figs. ~~11~~ 10), compared to the reference model using contact elements. Even, if the number of elements representing the fault zone is increased to nine (Figs. 11), the stress pattern is hardly different (~~Fig. 11~~). ~~Only narrow~~. Only close to the fault, a stress drop can be observed for ~~S_{Hmax} , S_{hmin} and S_v~~ S_{Hmax} , S_{hmin} and S_v . The von Mises stress ~~rises~~ increases locally, as the ~~S_{Hmax} – S_{Hmax}~~ decrease is lower than for ~~S_{hmin} and S_v~~ S_{hmin} and S_v . Localised swing-in effects can be observed; ~~from the extend~~, from the extent, most probably an artefact of the mesh resolution.

445 Fault zones are a 3-D structure consisting of the fault core and the damage zone (Caine et al., 1996; Chester and Logan, 1986; Faulkner et al., 1996; Chester and Logan, 1986; Caine et al., 1996; Faulkner et al., 2003, 2006). Previous work suggests, that the Young's modulus of the host rock decreases towards the damage zone, where the Poisson's ratio increases in the same way (Faulkner et al., 2006; Casey, 1980; Isaacs et al., 2008) (Casey, 1980; Faulkner et al., 2006; Isaacs et al., 2008). However, the variation of the Poisson's ratio is not tested here. Observed reduction of Young's modulus is from 55.4 GPa down to 16.2 GPa (Isaacs et al., 2008) or a reduction of about 6.5 GPa, e.g., from 66 GPa to 59.5 GPa (Faulkner et al., 2006). The here investigated range from $E = 15$ GPa to 0.125 GPa covers a large material property range. According Treffeisen and Henk (2020a), the amount of Young's modulus contrast have a strong impact on the resulting stress perturbation. Overall, this method the fault representation by means of elastically soft elements did not provide a stress pattern like as the contact surface method. Therefore, the representation of a fault by did. It is probable that representing a fault using only elastic weak elements only is apparent rather a method to dissipate stresses, but not to represent is a method of stress dissipation rather than an accurate representation of low friction faults properly.

4.3.2 Friction variation within the 3-D elements

The models having a 3-D-representation of the fault with a lateral variable number of elements, are allowed to fail according to the Mohr-Coulomb-Criteria. The resulting stress state by a friction angle of $\phi = 30^\circ$ and a cohesion of $C = 0.1$ kPa did not show much difference (Fig. 13) did not show much difference, compared to a model without a fault representation. Magnitude changes are in the order of less than 1 MPa next to the fault zone. The models with a lower friction displays larger ($\phi = 25, 20$ and 15°) displays larger stress perturbation in the vicinity of the fault (Fig. 14). The magnitude of stress perturbation is larger for the model using a friction angle of 15° , compared to the reference model with contact surfaces. The overall pattern is complex, some of the trends are similar, but the stress magnitudes are not decoupled when crossing the fault zone. As previously discussed, a low friction can be assumed for present-day fault activity. However, resulting stress pattern patterns differ to the results using contact elements. The continuous mesh did finite element mesh does not allow a real mechanical decoupling. This is may be different for other methods such as DEM where resulting behaviour depends on the number of elements and the friction (Hunt et al., 2004).

4.3.3 Cohesion variation within the 3-D elements

470 Usually, the key driver between intact rock and the fault using the Mohr-Coulomb-failure criteria is not the friction coefficient, but the cohesion. Even from the modelling perspective, cohesion have has the largest impact (Treffeisen and Henk, 2020a) on the stress state. Therefore the, models with elements with that have elasto-plastic rheology use employ the same friction ($\phi = 30^\circ$ $\phi = 30^\circ$, or $\mu = 0.58$), but a very low cohesion $C = 0.1$ kPa for within the fault zone, in contrast of $C = 500$ to $C = 500$ kPa outside this area. This is also the case for elements with elasto-plastic rheology, even if the parallel number reaches eight elements when the number of parallel elements reaches eight.

4.4 Distance of ~~Stress~~stress disturbance to faults

4.4.1 Far-field vs. near field

We have not specified the exact distance for the far-field or near-field, as such a distance depends on the orientation, properties, and size of the fault as well as on given stress field in the surrounding model volume. Fig. 1 and the previous content suggests, that the far-field is beyond about 100 m to the fault for intact host rock. As the ratio of displacement to fault length is about 1:100 (Torabi and Berg, 2011), even for a fault with a length of 10 km, the fault off-set can be up to 100 m. Depending on the faulting type, a limited correlation between fault displacement and thickness of a damage zone can be observed (Childs et al., 2009; Torabi and Berg, 2011). But the thickness of the damage zone is limited to a maximum of several hundred meters (Faulkner et al., 2010; Savage and Brodsky, 2011). However, for faults with a wide damage zones the impact of such a zone on the host rock is unlikely to be greater than for narrow fault zones, using the distance from the damage zone as a measure.

The impact of the different modelling approaches on the stress state differs. But a significant stress perturbation is spatially limited to a distance of maximum ~~1.000–1.500~~1000–2000 m next to the fault. Fig. 24 provides an visual overview of modelling results. This major assumption is supported by several authors using different approaches from a more map-view perspective (Faulkner et al., 2006; Petit and Mattauer, 1995; Provost and Houston, 2001; Su and Stephansson, 1999; Yale, 2003)(Petit and Mattauer, 1995). Also, observations from wells support that, where the stress perturbation is usually <200 m away from the fault (Barton and Zoback, 1994; Stephansson and Ångman, 1986; Barton and Zoback, 1994; Brudy et al., 1997; Tamagawa and Pollard, 2008; Lin et al., 2010). A rotation of about 90° within less than ~~100 to~~ 200 m in the vicinity of a fault has been observed near the Taiwan Chelungpu-fault (Lin et al., 2010) or at the Lansjärv well (Sweden, Bjarnason et al., 1989).

Only models with an oblique fault orientation relative to the maximum compression can achieve significant S_{Hmax} rotation. Especially those models with a low friction ($\mu = 0.1$, Fig 19) show S_{Hmax} rotation of up to 14° next to the fault. However, at a distance of 1500 m the deviation is smaller than 5°, which is quite below the uncertainties of the stress orientation indicators. Only when the friction coefficient becomes unrealistically small for faults in the inter-seismic phase (<0.1), larger rotations can be observed by the models at a distances of >1500 m away from the fault.

The relative stress state affects the spatial stress perturbation (Pollard and Segall, 1987). Therefore, Yale (2003) assumes, that in the case of low differential stress, the spatial ~~extend~~extent of stress perturbation is able to be ~~observe~~observed for up to several kilometres away from the fault. This fits in general to the results of the models varying the lateral strain, where the stress magnitude variation near the faults increases with a larger differential stress. Some previous models show more spacious far-field stress perturbations (Camae and Hunt, 2009; Sánchez D. et al., 1999; Tommasi et al., 1995)(Tommasi et al., 1995; Sánchez D. et al., 1999), which are most probably an artefact of a too coarse mesh resolution.

4.4.2 Vertical rotation of the stress tensor

Usage of the reduced stress tensor (S_{Hmax} , S_{Hmin} and S_V) is based on the assumption, that S_V is a principal stress. However, near to a weak and non-vertical fault, the principal stress orientation will be vertically distracted, as principal stresses are

510 always parallel to oblique to a free surface. This leads to a variation of all reduced stress components, including the shown S_V magnitudes. In the case of a thrust faulting- or strike-slip regime, S_V will be larger in the hanging wall block, and smaller in the footwall block, next to the fault (e.g. Fig 5). The opposite can be seen for a normal faulting regime, e.g. stress plots at greater depth (Fig. 7 at -2800 m).

4.5 Magnitude of stress perturbation

A decrease of horizontal stresses near the faults in the hanging wall, and an increase in the footwall is reported for the Forsmark
515 DBT 1 well (Sweden, Stephansson and Ångman, 1986). Less borehole breakouts in the hanging wall block and more in the footwall block are observed from the KTB well (Germany, Barton and Zoback, 1994). A reduction of σ_3 by about 5 MPa has been observed within less than 10 m near a tunnel at the Grimsel test site (Switzerland, Krietsch et al., 2019). All these observations fit to the results of the models having a fault representation by contact elements, where the horizontal stresses are smaller above the fault (Fig. 25), and the horizontal differential stress is smaller in the hanging wall block (Fig. 26). The latter
520 would make the occurrence of borehole breakouts less likely in the hanging wall.

In contrast to that, larger horizontal stresses above a fault have been observed for the Lansjärv well (Sweden, Bjarnason et al., 1989). The maximum horizontal stresses are observed about 100 m above the fault in the hanging wall block, which points also to other causes. One possible explanation is the lithological variation in ~~the-that~~ well, where several pegmatites and amphibolites in that depth range ~~has-have~~ been observed (Bjarnason et al., 1989), which eventually provide larger magnitudes
525 as a result of a larger Young's modulus.

According to Su and Stephansson (1999) is the magnitude variation positive correlated with the stress ratio and negative correlated with the friction. This can be clearly confirmed by this study (Figs. 8 and 23), where the stress variation near fault is largest for low friction models and models with a larger strain variation. Observation indicate that stresses decrease near a fault after an earthquake (~~Li et al., 2023; Zhou et al., 2012; Wang et al., 2015~~)(Zhou et al., 2012; Wang et al., 2015; Li et al., 2023).
530 This can be confirmed by the models for the hanging wall, but not for the footwall block. Either the observations are from the hanging wall block only, or other factors, like the 3-D structure, are responsible, which are not represented by the models, used here.

4.6 Other potential factors

~~Stress changes near the fault tip led to a complex stress pattern (Segall and Pollard, 1980; Rispoli, 1981; Homberg et al., 1997) --To mimic that, using only linear elastic material properties would lead to wrong assumptions. Therefore, such structures are not considered here. However, it can be assumed that stress changes induced by fault tips are negligible at distances of a few kilometres from the fault (Segall and Pollard, 1980; Su and Stephansson, 1999)~~All models analyse the variation of stress components and the orientation towards generic models with only one homogeneous fault. The extent to which the results can be applied to other scenarios remains questionable. There are some scenarios where we assume that other factors could
540 have a greater influence on the stress state. These include extensive settings such as horst- and graben structures, listric faults or step-over zones. In such cases, whole blocks may be completely decoupled, either by faults or by any kind of decoupling

horizon (salt, wet clay or pore over-pressure). The stress state in such a block is then dominated by gravity only. One potential example of this is the Arches National Park in Utah, USA, where the joints are almost perpendicular to the normal faults and are constant over several hundred metres (Kattenhorn et al., 2000). Secondary faulting also provides a possible explanation for the complex stress pattern within the Viking Graben (North Sea, Maerten et al., 2002). According to Siler (2023), large stress perturbations can be caused by a fault step-over structure in a hydrothermal systems over a distance of more than 1000 m in the Great Basin, western United States.

~~Several other potential geometrical reasons of stress perturbation are not tested here. For example, the curvature (e.g., listric fault) or roughness of the fault.~~ Faults or fault zones in nature are never as planar structures, as assumed by the presented models. Roughness plays a role, but the roughness in the direction of previous slip is much less, than in other directions (Power et al., 1987). The geometrical complexity are a result of non-planarity (bending, listric, bifurcation), combination or coalesce of faults (step-over- or relay zones) or others (e.g. Roche et al., 2021). Fault zones can exist out of several single parallel faults, which probably would produce a wider distributed area of stress perturbation. Pore pressure, especially ~~overpressure, can have a large potential on the stress state (Blanpied et al., 1992; Byerlee, 1993), above hydro-static has a~~ significant impact on ~~the fault behaviour. But this has~~ effective fault normal stresses (Blanpied et al., 1992; Byerlee, 1993). Despite the large number of models presented, such complex structures or properties have not been tested here.

Stress changes near the fault tip (e.g. horsetail fault terminations) led to a complex stress pattern (Segall and Pollard, 1980; Rispoli, 1981). To model that, using only linear elastic material properties would result in unrealistic local stress peaks as elastic energy would not be dissipated by plastic deformation. Therefore, such structures are not considered here. However, it can be assumed that stress changes induced by fault tips are negligible at distances of a few kilometres from the fault (Segall and Pollard, 1980; Su and Stephans

5 Conclusions

The results of our study show that the static fault friction coefficient, rock strength, stiffness and density contrast of the fault significantly affect the stress tensor beyond the fault core. However, the stress magnitudes as well as stress tensor orientation is not significantly changed beyond a distance of about ~~1.000 or 1.500~~ 1000 m. S_{Hmax} rotation is only observable when the overall orientation of S_{Hmax} is oblique to the fault strike and the static friction coefficient is low (e.g. $\mu = 0.1$). From these findings we can conclude that ~~most of~~

~~many of~~ the stress tensor rotations that are documented in recent publications based on high density data sets (Heidbach et al., 2007; Lund ~~are very much likely~~ (Heidbach et al., 2007; Pierdominici and Heidbach, 2012; Rajabi et al., 2016, 2017b; Lund Snee and Zoback, 2018, 2020) are probably not controlled by faults, ~~but rather rock property variability (e.g., Reiter, 2021), by~~. Other factors probably play a greater role, like variable rock property (e.g., Reiter, 2021) or the superposition of plate boundary forces with different orientation and magnitude ~~, or a mixture of both (Ferreira et al., 1998; Rajabi et al., 2017a) (Ferreira et al., 1998; Rajabi et al., 2017a)~~. Specific fault setting could also play a roll, like decoupled graben blocks (Ferreira et al., 1998; Rajabi et al., 2017a) or secondary

575 faults in extensional settings (Maerten et al., 2002), fault termination or transfer zones (Siler, 2023). However, it is doubtful that their far-field effect extends beyond 10 km.

Symbols

Table 3. Explanation of the symbols used

C	Cohesion
DEM	Discret Element Method
E	Youngs -Young's Modulus
<u>FDM</u>	<u>Finite Difference Method</u>
FEM	Finite Element Method
<u>FVM</u>	<u>Finite Volume Method</u>
g	Gravitational acceleration
S_{Hmax}	Maximum horizontal stress
S_{hmin}	Minimum horizontal stress
S_V	Vertical stress
X, Y, Z	Coordinates (cartesian)
z	Depth
ϵ	Strain
μ	Static friction coefficient
ν	Poisson's ratio
ρ	Density
σ	Stress tensor
σ_1	Largest principal stress
σ_2	Intermediate principal stress
σ_3	Least principal stress
σ_D	Differential stress
σ_{vM}	von Mises stress
ϕ	Friction angle
ψ	Dilation angle

Author contributions. KR: study set-up, model preparation, writing, discussion, OH: study set-up, discussion MZ: discussion

Competing interests. The contact author has declared that none of the authors has any competing interests.

Acknowledgements. Some of the results of that study was first presented in Heidbach and Reiter (2019). This study was partly funded by the
580 National Cooperative for the Disposal of Radioactive Waste (Nagra), Switzerland and the Bundesgesellschaft für Endlagerung (BGE) within
the project SpannEnD II (www.spannend-projekt.de).

References

- Anderson, E. M.: The dynamics of faulting, *Transactions of the Edinburgh Geological Society*, 8, 387–402, <https://doi.org/10.1144/transed.8.3.387>, 1905.
- 585 Anderson, E. M.: *The Dynamics of Faulting and Dyke Formation with Application to Britain*, 2nd ed. Oliver and Boyd, London and Edinburgh, 1951.
- Barton, C. A. and Zoback, M. D.: Stress perturbations associated with active faults penetrated by boreholes: Possible evidence for near-complete stress drop and a new technique for stress magnitude measurement, *Journal of Geophysical Research: Solid Earth*, 99, 9373–9390, <https://doi.org/10.1029/93JB03359>, 1994.
- 590 Bell, J. S.: In situ stresses in sedimentary rocks (part 2): Applications of stress measurements, *Geoscience Canada*, 23, 135–153, <http://journals.hil.unb.ca/index.php/GC/article/view/3910>, 1996.
- Bird, P. and Xianghong Kong: Computer simulations of California tectonics confirm very low strength of major faults, *Geological Society of America Bulletin*, 106, 159–174, [https://doi.org/10.1130/0016-7606\(1994\)106<0159:CSOCTC>2.3.CO;2](https://doi.org/10.1130/0016-7606(1994)106<0159:CSOCTC>2.3.CO;2), 1994.
- Bjarnason, B., Zellman, O., and Wikberg, P.: Drilling and borehole description, in: *Interdisciplinary study of post-glacial faulting in the*
- 595 *Lansjärv area Northern Sweden 1986 - 1988*, edited by Bäckblom, G. and Stanfors, R., chap. 7, pp. 7:1–7:14, Svensk Kärnbränslehantering Aktiefbolag (SKB), skb tr 89- edn., 1989.
- Blanpied, M. L., Lockner, D. A., and Byerlee, J. D.: An earthquake mechanism based on rapid sealing of faults, *Nature*, 358, 574–576, <https://doi.org/10.1038/358574a0>, 1992.
- Blöcher, G., Cacace, M., Jacquey, A. B., Zang, A., Heidbach, O., Hofmann, H., Kluge, C., and Zimmermann, G.: Evaluating Micro-Seismic
- 600 *Events Triggered by Reservoir Operations at the Geothermal Site of Groß Schönebeck (Germany)*, *Rock Mechanics and Rock Engineering*, 51, 3265–3279, <https://doi.org/10.1007/s00603-018-1521-2>, 2018.
- Boulton, C., Yao, L., Faulkner, D. R., Townend, J., Toy, V. G., Sutherland, R., Ma, S., and Shimamoto, T.: High-velocity frictional properties of Alpine Fault rocks: Mechanical data, microstructural analysis, and implications for rupture propagation, *Journal of Structural Geology*, 97, 71–92, <https://doi.org/10.1016/j.jsg.2017.02.003>, 2017.
- 605 Brace, W. F. and Kohlstedt, D. L.: Limits on lithospheric stress imposed by laboratory experiments, *Journal of Geophysical Research*, 85, 6248, <https://doi.org/10.1029/JB085iB11p06248>, 1980.
- Brodsky, E. E., Mori, J. J., Anderson, L., Chester, F. M., Conin, M., Dunham, E. M., Eguchi, N., Fulton, P. M., Hino, R., Hirose, T., Ikari, M. J., Ishikawa, T., Jeppson, T., Kano, Y., Kirkpatrick, J., Kodaira, S., Lin, W., Nakamura, Y., Rabinowitz, H. S., Regalla, C., Remitti, F., Rowe, C., Saffer, D. M., Saito, S., Sample, J., Sanada, Y., Savage, H. M., Sun, T., Toczko, S., Ujiie, K., Wolfson-Schwehr, M., and Yang,
- 610 T.: The State of Stress on the Fault Before, During, and after a Major Earthquake, <https://doi.org/10.1146/annurev-earth-053018-060507>, 2020.
- Brudy, M., Zoback, M. D., Fuchs, K., Rummel, F., and Baumgärtner, J.: Estimation of the complete stress tensor to 8 km depth in the KTB scientific drill holes: Implications for crustal strength, *Journal of Geophysical Research: Solid Earth*, 102, 18453–18475, <https://doi.org/10.1029/96JB02942>, 1997.
- 615 Buchmann, T. J. and Connolly, P. T.: Contemporary kinematics of the Upper Rhine Graben: A 3D finite element approach, *Global and Planetary Change*, 58, 287–309, <https://doi.org/10.1016/j.gloplacha.2007.02.012>, 2007.
- Burov, E. B. and Diament, M.: The effective elastic thickness (T_e) of continental lithosphere: what does it really mean?, *Journal of Geophysical Research*, 100, 3905–3927, <https://doi.org/10.1029/94JB02770>, 1995.

- Byerlee, J.: Friction of Rocks, *Pure and Applied Geophysics PAGEOPH*, 116, 615–626, <https://doi.org/10.1007/BF00876528>, 1978.
- 620 Byerlee, J.: Model for episodic flow of high-pressure water in fault zones before earthquakes, *Geology*, 21, 303–306, [https://doi.org/10.1130/0091-7613\(1993\)021<0303:MFEFOH>2.3.CO;2](https://doi.org/10.1130/0091-7613(1993)021<0303:MFEFOH>2.3.CO;2), 1993.
- Caine, J. S., Evans, J. P., and Forster, C. B.: Fault zone architecture and permeability structure, *Geology*, 24, 1025, [https://doi.org/10.1130/0091-7613\(1996\)024<1025:FZAAPS>2.3.CO;2](https://doi.org/10.1130/0091-7613(1996)024<1025:FZAAPS>2.3.CO;2), 1996.
- Camac, B. A. and Hunt, S. P.: Predicting the regional distribution of fracture networks using the distinct element numerical method, *AAPG Bulletin*, 93, 1571–1583, <https://doi.org/10.1306/07230909040>, 2009.
- 625 Cappa, F.: Modelling fluid transfer and slip in a fault zone when integrating heterogeneous hydromechanical characteristics in its internal structure, *Geophysical Journal International*, 178, 1357–1362, <https://doi.org/10.1111/j.1365-246X.2009.04291.x>, 2009.
- Cappa, F. and Rutqvist, J.: Impact of CO₂ geological sequestration on the nucleation of earthquakes, *Geophysical Research Letters*, 38, 2–7, <https://doi.org/10.1029/2011GL048487>, 2011.
- 630 Carena, S. and Moder, C.: The strength of faults in the crust in the western United States, *Earth and Planetary Science Letters*, 287, 373–384, <https://doi.org/10.1016/j.epsl.2009.08.021>, 2009.
- Carpenter, B. M., Saffer, D. M., and Marone, C.: Frictional properties of the active San Andreas Fault at SAFOD: Implications for fault strength and slip behavior, *Journal of Geophysical Research: Solid Earth*, 120, 5273–5289, <https://doi.org/10.1002/2015JB011963>, 2015.
- Casey, M.: Mechanics of shear zones in isotropic dilatant materials, *Journal of Structural Geology*, 2, 143–147, [https://doi.org/10.1016/0191-8141\(80\)90044-9](https://doi.org/10.1016/0191-8141(80)90044-9), 1980.
- 635 Chéry, J., Zoback, M. D., and Hickman, S.: A mechanical model of the San Andreas fault and SAFOD Pilot Hole stress measurements, *Geophysical Research Letters*, 31, 1–6, <https://doi.org/10.1029/2004GL019521>, 2004.
- Chester, F. M. and Logan, J. M.: Implications for mechanical properties of brittle faults from observations of the Punchbowl fault zone, California, *Pure and Applied Geophysics*, 124, 79–106, <https://doi.org/10.1007/BF00875720>, 1986.
- 640 Childs, C., Manzocchi, T., Walsh, J. J., Bonson, C. G., Nicol, A., and Schöpfer, M. P. J.: A geometric model of fault zone and fault rock thickness variations, *Journal of Structural Geology*, 31, 117–127, <https://doi.org/10.1016/j.jsg.2008.08.009>, 2009.
- Cundall, P. A. and Hart, R. D.: Numerical Modelling of Discontinua, *Engineering Computations*, 9, 101–113, <https://doi.org/10.1108/eb023851>, 1992.
- Dart, R. L. and Swolfs, H. S.: Subparallel faults and horizontal-stress orientations: An evaluation of in-situ stresses inferred from elliptical wellbore enlargements, *Norwegian Petroleum Society Special Publications*, 1, 519–529, <https://doi.org/10.1016/B978-0-444-88607-1.50041-3>, 1992.
- 645 de Jossineau, G., Petit, J. P., and Gauthier, B. D.: Photoelastic and numerical investigation of stress distributions around fault models under biaxial compressive loading conditions, *Tectonophysics*, 363, 19–43, [https://doi.org/10.1016/S0040-1951\(02\)00648-0](https://doi.org/10.1016/S0040-1951(02)00648-0), 2003.
- Delogkos, E., Roche, V., and Walsh, J. J.: Bed-parallel slip associated with normal fault systems, *Earth-Science Reviews*, 230, 104 044, <https://doi.org/10.1016/j.earscirev.2022.104044>, 2022.
- 650 Desroches, J., Peyret, E., Gisolf, A., Wilcox, A., Giovanni, M. D., de Jong, A. S., Sepehri, S., Garrard, R., and Giger, S.: Stress Measurement Campaign in Scientific Deep Boreholes: Focus on Tool and Methods, in: SPWLA 62nd Annual Logging Symposium, <https://doi.org/10.30632/spwla-2021-0056>, 2021.
- Di Toro, G., Han, R., Hirose, T., De Paola, N., Nielsen, S., Mizoguchi, K., Ferri, F., Cocco, M., and Shimamoto, T.: Fault lubrication during earthquakes, *Nature*, 471, 494–499, <https://doi.org/10.1038/nature09838>, 2011.
- 655

- Faulkner, D. R., Lewis, A. C., and Rutter, E. H.: On the internal structure and mechanics of large strike-slip fault zones: Field observations of the Carboneras fault in southeastern Spain, *Tectonophysics*, 367, 235–251, [https://doi.org/10.1016/S0040-1951\(03\)00134-3](https://doi.org/10.1016/S0040-1951(03)00134-3), 2003.
- Faulkner, D. R., Mitchell, T. M., Healy, D., and Heap, M. J.: Slip on 'weak' faults by the rotation of regional stress in the fracture damage zone, *Nature*, 444, 922–925, <https://doi.org/10.1038/nature05353>, 2006.
- 660 Faulkner, D. R., Jackson, C. A., Lunn, R. J., Schlische, R. W., Shipton, Z. K., Wibberley, C. A., and Withjack, M. O.: A review of recent developments concerning the structure, mechanics and fluid flow properties of fault zones, *Journal of Structural Geology*, 32, 1557–1575, <https://doi.org/10.1016/j.jsg.2010.06.009>, 2010.
- Ferreira, J. M., Oliveira, R. T., Takeya, M. K., and Assumpção, M.: Superposition of local and regional stresses in northeast Brazil: evidence from focal mechanisms around the Potiguar marginal basin, *Geophysical Journal International*, 134, 341–355, <https://doi.org/10.1046/j.1365-246X.1998.00563.x>, 1998.
- 665 Ferrill, D. A., Smart, K. J., and Morris, A. P.: Fault failure modes, deformation mechanisms, dilation tendency, slip tendency, and conduits v. Seals, *Geological Society Special Publication*, 496, 75–98, <https://doi.org/10.1144/SP496-2019-7>, 2020.
- Fitzenz, D. D. and Miller, S. A.: A forward model for earthquake generation on interacting faults including tectonics, fluids, and stress transfer, *Journal of Geophysical Research: Solid Earth*, 106, 26 689–26 706, <https://doi.org/10.1029/2000jb000029>, 2001.
- 670 Franceschini, A., Ferronato, M., Janna, C., and Teatini, P.: A novel Lagrangian approach for the stable numerical simulation of fault and fracture mechanics, *Journal of Computational Physics*, 314, 503–521, <https://doi.org/10.1016/j.jcp.2016.03.032>, 2016.
- Fuchs, K. and Müller, B.: World Stress Map of the Earth: a key to tectonic processes and technological applications, *Naturwissenschaften*, 88, 357–371, <https://doi.org/10.1007/s001140100253>, 2001.
- Fulton, P. M., Brodsky, E. E., Kano, Y., Mori, J., Chester, F., Ishikawa, T., Harris, R. N., Lin, W., Eguchi, N., and Toczko, S.: Low coseismic friction on the Tohoku-Oki fault determined from temperature measurements, *Science*, 342, 1214–1217, <https://doi.org/10.1126/science.1243641>, 2013.
- 675 Hafner, W.: Stress distributions and faulting, *Bulletin of the Geological Society of America*, 62, 373–398, [https://doi.org/10.1130/0016-7606\(1951\)62\[373:SDAF\]2.0.CO;2](https://doi.org/10.1130/0016-7606(1951)62[373:SDAF]2.0.CO;2), 1951.
- Hardebeck, J. L. and Okada, T.: Temporal Stress Changes Caused by Earthquakes: A Review, *Journal of Geophysical Research: Solid Earth*, 123, 1350–1365, <https://doi.org/10.1002/2017JB014617>, 2018.
- 680 Heidbach, O. and Ben-Avraham, Z.: Stress evolution and seismic hazard of the Dead Sea Fault System, *Earth and Planetary Science Letters*, 257, 299–312, <https://doi.org/10.1016/j.epsl.2007.02.042>, 2007.
- Heidbach, O. and Reiter, K.: Interner Bericht NIB 19-15 - Impact of fault properties and fault implementation strategies on results of 3D geomechanical-numerical models, Tech. Rep. March, NAGRA, Wettingen, 2019.
- 685 Heidbach, O., Barth, A., Connolly, P. T., Fuchs, K., Müller, B., Tingay, M., Reinecker, J., Spencer, B., and Wenzel, F.: Stress Maps in a Minute: The 2004 World Stress Map Release, *Eos, Transactions American Geophysical Union*, 85, 521, <https://doi.org/10.1029/2001GC000252>.Fuchs, 2004.
- Heidbach, O., Reinecker, J., Tingay, M., Müller, B., Sperner, B., Fuchs, K., and Wenzel, F.: Plate boundary forces are not enough: Second- and third-order stress patterns highlighted in the World Stress Map database, *Tectonics*, 26, 1–19, <https://doi.org/10.1029/2007TC002133>, 2007.
- 690 Heidbach, O., Rajabi, M., Cui, X., Fuchs, K., Müller, B., Reinecker, J., Reiter, K., Tingay, M., Wenzel, F., Xie, F., Ziegler, M. O., Zoback, M.-L., and Zoback, M. D.: The World Stress Map database release 2016: Crustal stress pattern across scales, *Tectonophysics*, 744, 484–498, <https://doi.org/10.1016/j.tecto.2018.07.007>, 2018.

- Henk, A.: Numerical modelling of faults, in: *Understanding Faults*, chap. 4, p. 2, Elsevier, <https://doi.org/10.1016/b978-0-12-815985-9.00004-7>, 2020.
- 695 Hergert, T. and Heidbach, O.: Geomechanical model of the Marmara Sea region-II. 3-D contemporary background stress field, *Geophysical Journal International*, 185, 1090–1102, <https://doi.org/10.1111/j.1365-246X.2011.04992.x>, 2011.
- Hergert, T., Heidbach, O., Bécel, A., and Laigle, M.: Geomechanical model of the Marmara Sea region-I. 3-D contemporary kinematics, *Geophysical Journal International*, 185, 1073–1089, <https://doi.org/10.1111/j.1365-246X.2011.04991.x>, 2011.
- 700 Hergert, T., Heidbach, O., Reiter, K., Giger, S. B., and Marschall, P.: Stress Field Sensitivity Analysis at a Reservoir Scale (Northern Switzerland) Using Numerical Geomechanical Modelling, *Solid Earth*, 6, 533–552, <https://doi.org/10.5194/se-6-533-2015>, 2015.
- Hickman, S. and Zoback, M.: Stress orientations and magnitudes in the SAFOD pilot hole, *Geophysical Research Letters*, 31, L15S12, <https://doi.org/10.1029/2004GL020043>, 2004.
- Homberg, C., Hu, J., Angelier, J., Bergerat, F., and Lacombe, O.: Characterization of stress perturbations near major fault zones: insights from 2-D distinct-element numerical modelling and field studies (Jura mountains), *Journal of Structural Geology*, 19, 703–718, [https://doi.org/10.1016/S0191-8141\(96\)00104-6](https://doi.org/10.1016/S0191-8141(96)00104-6), 1997.
- 705 Houston, H.: Low friction and fault weakening revealed by rising sensitivity of tremor to tidal stress, *Nature Geoscience*, 8, 409–415, <https://doi.org/10.1038/ngeo2419>, 2015.
- Hudson, J. A. and Cooling, C. M.: In Situ rock stresses and their measurement in the U.K.-Part I. The current state of knowledge, *International Journal of Rock Mechanics and Mining Sciences and*, 25, 363–370, [https://doi.org/10.1016/0148-9062\(88\)90976-X](https://doi.org/10.1016/0148-9062(88)90976-X), 1988.
- 710 Hunt, S. P., Camac, B. A., and Boulton, P.: A parametric analysis and applications of the discrete element method for stress modeling, in: *Proceedings of the 9th Australia New Zealand Conference on Geomechanics*, Auckland, p. 7, 2004.
- Hyndman, R. D., Currie, C. A., Mazzotti, S., and Frederiksen, A.: Temperature control of continental lithosphere elastic thickness, *Te vs Vs, Earth and Planetary Science Letters*, 277, 539–548, <https://doi.org/10.1016/j.epsl.2008.11.023>, 2009.
- 715 Iaffaldano, G.: The strength of large-scale plate boundaries: Constraints from the dynamics of the Philippine Sea plate since ~5Ma, *Earth and Planetary Science Letters*, 357-358, 21–30, <https://doi.org/10.1016/j.epsl.2012.09.018>, 2012.
- Isaacs, A. J., Evans, J. P., Kolesar, P. T., and Nohara, T.: Composition, microstructures, and petrophysics of the Mozumi fault, Japan: In situ analyses of fault zone properties and structure in sedimentary rocks from shallow crustal levels, *Journal of Geophysical Research*, 113, B12 408, <https://doi.org/10.1029/2007JB005314>, 2008.
- 720 Jaeger, J. C., Cook, N., and Zimmerman, R.: *Fundamentals of rock mechanics*, Blackwell, Hoboken, New Jersey, 4th edn., 2011.
- Kattenhorn, S. A., Aydin, A., and Pollard, D. D.: Joints at high angles to normal fault strike: An explanation using 3-D numerical models of fault-perturbed stress fields, *Journal of Structural Geology*, 22, 1–23, [https://doi.org/10.1016/S0191-8141\(99\)00130-3](https://doi.org/10.1016/S0191-8141(99)00130-3), 2000.
- Konstantinovskaia, E., Malo, M., and Castillo, D. A.: Present-day stress analysis of the St. Lawrence Lowlands sedimentary basin (Canada) and implications for caprock integrity during CO₂ injection operations, *Tectonophysics*, 518-521, 119–137, <https://doi.org/10.1016/j.tecto.2011.11.022>, 2012.
- 725 Krietsch, H., Gischig, V., Evans, K., Doetsch, J., Dutler, N. O., Valley, B., and Amann, F.: Stress Measurements for an In Situ Stimulation Experiment in Crystalline Rock: Integration of Induced Seismicity, Stress Relief and Hydraulic Methods, *Rock Mechanics and Rock Engineering*, 52, 517–542, <https://doi.org/10.1007/s00603-018-1597-8>, 2019.
- Kruszewski, M., Klee, G., Niederhuber, T., and Heidbach, O.: In situ stress database of the greater Ruhr region (Germany) derived from
- 730 hydrofracturing tests and borehole logs, *Earth System Science Data*, 14, 5367–5385, <https://doi.org/10.5194/essd-14-5367-2022>, 2022.

- Li, P., Cai, M., Gorjjan, M., Ren, F., Xi, X., and Wang, P.: Interaction between in situ stress states and tectonic faults: A comment, <https://doi.org/10.1007/s12613-023-2607-8>, 2023.
- 735 Lin, W., Yeh, E. C., Hung, J.-H., Haimson, B. C., and Hirono, T.: Localized rotation of principal stress around faults and fractures determined from borehole breakouts in hole B of the Taiwan Chelungpu-fault Drilling Project (TCDP), *Tectonophysics*, 482, 82–91, <https://doi.org/10.1016/j.tecto.2009.06.020>, 2010.
- Lin, W., Conin, M., Moore, J. C., Chester, F. M., Nakamura, Y., Mori, J. J., Anderson, L., Brodsky, E. E., Eguchi, N., Cook, B., Jeppson, T., Wolfson-Schwehr, M., Sanada, Y., Saito, S., Kido, Y., Hirose, T., Behrmann, J. H., Ikari, M., Ujiie, K., Rowe, C., Kirkpatrick, J., Bose, S., Regalla, C., Remitti, F., Toy, V., Fulton, P., Mishima, T., Yang, T., Sun, T., Ishikawa, T., Sample, J., Takai, K., Kameda, J., Toczko, S., Maeda, L., Kodaira, S., Hino, R., and Saffer, D.: Stress state in the largest displacement area of the 2011 Tohoku-Oki earthquake, *Science*, 740 339, 687–690, <https://doi.org/10.1126/science.1229379>, 2013.
- Lockner, D. A., Morrow, C., Moore, D., and Hickman, S. H.: Low strength of deep San Andreas fault gouge from SAFOD core., *Nature*, 472, 82–85, <https://doi.org/10.1038/nature09927>, 2011.
- Lund Snee, J.-E. and Zoback, M. D.: State of stress in the Permian Basin, Texas and New Mexico: Implications for induced seismicity, *Leading Edge*, 37, 127–134, <https://doi.org/10.1190/tle37020127.1>, 2018.
- 745 Lund Snee, J.-E. and Zoback, M. D.: Multiscale variations of the crustal stress field throughout North America, *Nature Communications*, 11, 1951, <https://doi.org/10.1038/s41467-020-15841-5>, 2020.
- Maerten, L., Gillespie, P., and Pollard, D. D.: Effects of local stress perturbation on secondary fault development, *Journal of Structural Geology*, 24, 145–153, [https://doi.org/10.1016/S0191-8141\(01\)00054-2](https://doi.org/10.1016/S0191-8141(01)00054-2), 2002.
- Maerten, L., Maerten, F., Lejri, M., and Gillespie, P.: Geomechanical paleostress inversion using fracture data, *Journal of Structural Geology*, 750 89, 197–213, <https://doi.org/10.1016/j.jsg.2016.06.007>, 2016.
- McLellan, J. G., Oliver, N. H., and Schaub, P. M.: Fluid flow in extensional environments; numerical modelling with an application to Hamersley iron ores, *Journal of Structural Geology*, 26, 1157–1171, <https://doi.org/10.1016/j.jsg.2003.11.015>, 2004.
- Meier, S., Bauer, J. F., and Philipp, S. L.: Fault zones in layered carbonate successions: from field data to stress field models, *Geomechanics and Geophysics for Geo-Energy and Geo-Resources*, 3, 61–93, <https://doi.org/10.1007/s40948-016-0047-x>, 2017.
- 755 Mises, R. v.: *Mechanik der festen Körper im plastisch- deformablen Zustand*, Nachrichten von der Gesellschaft der Wissenschaften zu Göttingen, Mathematisch-Physikalische Klasse, 1913, 582–592, <http://eudml.org/doc/58894>, 1913.
- Moeck, I. and Backers, T.: Fault reactivation potential as a critical factor during reservoir stimulation, *First Break*, 29, 73–80, <https://doi.org/10.3997/1365-2397.2011014>, 2011.
- Morris, A. P., Ferrill, D. A., and Henderson, D. B.: Slip-tendency analysis and fault reactivation, *Geology*, 24, 275–278, 760 [https://doi.org/10.1130/0091-7613\(1996\)024<0275:STAAFR>2.3.CO;2](https://doi.org/10.1130/0091-7613(1996)024<0275:STAAFR>2.3.CO;2), 1996.
- Mount, V. S. and Suppe, J.: State of stress near the San Andreas fault: Implications for wrench tectonics, *Geology*, 15, 1143, [https://doi.org/10.1130/0091-7613\(1987\)15<1143:SOSNTS>2.0.CO;2](https://doi.org/10.1130/0091-7613(1987)15<1143:SOSNTS>2.0.CO;2), 1987.
- Mount, V. S. and Suppe, J.: Present-day stress orientations adjacent to active strike-slip faults: California and Sumatra, *Journal of Geophysical Research*, 97, 11 995, <https://doi.org/10.1029/92JB00130>, 1992.
- 765 Muhuri, S. K., Dewers, T. A., Scott Thurman E., J. E., and Reches, Z.: Interseismic fault strengthening and earthquake-slip instability: Friction or cohesion?, *Geology*, 31, 881–884, <https://doi.org/10.1130/G19601.1>, 2003.
- Osokina, D.: Hierarchical properties of a stress field and its relation to fault displacements, *Journal of Geodynamics*, 10, 331–344, [https://doi.org/10.1016/0264-3707\(88\)90039-7](https://doi.org/10.1016/0264-3707(88)90039-7), 1988.

- Pereira, L. C., Guimarães, L. J., Horowitz, B., and Sánchez, M.: Coupled hydro-mechanical fault reactivation analysis incorporating evidence
770 theory for uncertainty quantification, *Computers and Geotechnics*, 56, 202–215, <https://doi.org/10.1016/j.compgeo.2013.12.007>, 2014.
- Petit, J. P. and Mattauer, M.: Palaeostress superimposition deduced from mesoscale structures in limestone: the Matelles exposure, Languedoc, France, *Journal of Structural Geology*, 17, 245–256, [https://doi.org/10.1016/0191-8141\(94\)E0039-2](https://doi.org/10.1016/0191-8141(94)E0039-2), 1995.
- Pierdominici, S. and Heidbach, O.: Stress field of Italy - Mean stress orientation at different depths and wave-length of the stress pattern, *Tectonophysics*, 532-535, 301–311, <https://doi.org/10.1016/j.tecto.2012.02.018>, 2012.
- 775 Pollard, D. D. and Segall, P.: Theoretical Displacements and Stresses Near Fractures in Rock: With Applications To Faults, Joints, Veins, Dikes, and Solution Surfaces, in: *Fracture Mechanics of Rock*, pp. 277–349, Elsevier, <https://doi.org/10.1016/b978-0-12-066266-1.50013-2>, 1987.
- Power, W. L., Tullis, T. E., Brown, S. R., Boitnott, G. N., and Scholz, C. H.: Roughness of natural fault surfaces, *Geophysical Research Letters*, 14, 29–32, <https://doi.org/10.1029/GL014i001p00029>, 1987.
- 780 Prévost, J. H. and Sukumar, N.: Faults simulations for three-dimensional reservoir-geomechanical models with the extended finite element method, *Journal of the Mechanics and Physics of Solids*, 86, 1–18, <https://doi.org/10.1016/j.jmps.2015.09.014>, 2016.
- Provost, A. S. and Houston, H.: Orientation of the stress field surrounding the creeping section of the San Andreas Fault: Evidence for a narrow mechanically weak fault zone, *Journal of Geophysical Research: Solid Earth*, 106, 11 373–11 386, <https://doi.org/10.1029/2001jb900007>, 2001.
- 785 Rajabi, M., Tingay, M., Heidbach, O., Hillis, R., and Reynolds, S. D.: The present-day stress field of Australia, *Earth-Science Reviews*, 168, 165–189, <https://doi.org/10.1016/j.earscirev.2017.04.003>, 2016.
- Rajabi, M., Heidbach, O., Tingay, M., and Reiter, K.: Prediction of the present-day stress field in the Australian continental crust using 3D geomechanical–numerical models, *Australian Journal of Earth Sciences*, 64, 435–454, <https://doi.org/10.1080/08120099.2017.1294109>, 2017a.
- 790 Rajabi, M., Tingay, M., Heidbach, O., Hillis, R., and Reynolds, S.: The present-day stress field of Australia, *Earth-Science Reviews*, 168, 165–189, <https://doi.org/10.1016/j.earscirev.2017.04.003>, 2017b.
- Rajabi, M., Tingay, M., King, R., and Heidbach, O.: Present-day stress orientation in the Clarence-Moreton Basin of New South Wales, Australia: a new high density dataset reveals local stress rotations, *Basin Research*, 29, 622–640, <https://doi.org/10.1111/bre.12175>, 2017c.
- Rawnsley, K. D., Rives, T., Petti, J. P., Hencher, S. R., and Lumsden, A. C.: Joint development in perturbed stress fields near faults, *Journal*
795 *of Structural Geology*, 14, 939–951, [https://doi.org/10.1016/0191-8141\(92\)90025-R](https://doi.org/10.1016/0191-8141(92)90025-R), 1992.
- Reiter, K.: Stress rotation – impact and interaction of rock stiffness and faults, *Solid Earth*, 12, 1287–1307, <https://doi.org/10.5194/se-12-1287-2021>, 2021.
- Reiter, K. and Heidbach, O.: 3-D geomechanical-numerical model of the contemporary crustal stress state in the Alberta Basin (Canada), *Solid Earth*, 5, 1123–1149, <https://doi.org/10.5194/se-5-1123-2014>, 2014.
- 800 Rispoli, R.: Stress fields about strike-slip faults inferred from stylolites and tension gashes, *Tectonophysics*, 75, 29–36, [https://doi.org/10.1016/0040-1951\(81\)90274-2](https://doi.org/10.1016/0040-1951(81)90274-2), 1981.
- Roche, V., Camanni, G., Childs, C., Manzocchi, T., Walsh, J., Conneally, J., Saqab, M. M., and Delogkos, E.: Variability in the three-dimensional geometry of segmented normal fault surfaces, *Earth-Science Reviews*, 216, 103 523, <https://doi.org/10.1016/j.earscirev.2021.103523>, 2021.
- 805 Röckel, L., Ahlers, S., Müller, B., Reiter, K., Heidbach, O., Henk, A., Hergert, T., and Schilling, F.: The analysis of slip tendency of major tectonic faults in Germany, *Solid Earth*, 13, 1087–1105, <https://doi.org/10.5194/se-13-1087-2022>, 2022.

- Sánchez D., M. A., Vásquez, A. R., Van Alstine, D., Butterworth, J., García, J., Carmona, R., Poquioma, W., and Ramones, M.: Applications of Geomechanics in the Development of the Naturally Fractured Carbonates of the Mara Oeste Field, Venezuela, in: Latin American and Caribbean Petroleum Engineering Conference, vol. SPE 54008, p. 8, SPE, Caracas, Venezuela, <https://doi.org/10.2118/54008-MS>, 1999.
- 810 Savage, H. M. and Brodsky, E. E.: Collateral damage: Evolution with displacement of fracture distribution and secondary fault strands in fault damage zones, *Journal of Geophysical Research: Solid Earth*, 116, <https://doi.org/10.1029/2010JB007665>, 2011.
- Schellart, W. P.: Shear test results for cohesion and friction coefficients for different granular materials: Scaling implications for their usage in analogue modelling, *Tectonophysics*, 324, 1–16, [https://doi.org/10.1016/S0040-1951\(00\)00111-6](https://doi.org/10.1016/S0040-1951(00)00111-6), 2000.
- Schoenball, M. and Davatzes, N. C.: Quantifying the heterogeneity of the tectonic stress field using borehole data, *Journal of Geophysical Research: Solid Earth*, 122, 6737–6756, <https://doi.org/10.1002/2017JB014370>, 2017.
- 815 Schoenball, M., Walsh, F. R., Weingarten, M., and Ellsworth, W. L.: How faults wake up: The Guthrie–Langston, Oklahoma earthquakes, *Leading Edge*, 37, 100–106, <https://doi.org/10.1190/tle37020100.1>, 2018.
- Schuite, J., Longuevergne, L., Bour, O., Burbey, T. J., Boudin, F., Lavenant, N., and Davy, P.: Understanding the Hydromechanical Behavior of a Fault Zone From Transient Surface Tilt and Fluid Pressure Observations at Hourly Time Scales, *Water Resources Research*, 53, 10 558–10 582, <https://doi.org/10.1002/2017WR020588>, 2017.
- 820 Segall, P. and Pollard, D. D.: Mechanics of discontinuous faults, *Journal of Geophysical Research: Solid Earth*, 85, 4337–4350, <https://doi.org/10.1029/jb085ib08p04337>, 1980.
- Seithel, R., Gaucher, E., Müller, B., Steiner, U., and Kohl, T.: Probability of fault reactivation in the Bavarian Molasse Basin, *Geothermics*, 82, 81–90, <https://doi.org/10.1016/j.geothermics.2019.06.004>, 2019.
- 825 Shi, H., Huang, F., Ma, Z., Wang, Y., Feng, J., and Gao, X.: Mechanical Mechanism of Fault Dislocation Based on in situ Stress State, *Frontiers in Earth Science*, 8, 1–9, <https://doi.org/10.3389/feart.2020.00052>, 2020.
- Siler, D. L.: Structural discontinuities and their control on hydrothermal systems in the Great Basin, USA, *Geoenergy*, 1, <https://doi.org/10.1144/geoenergy2023-009>, 2023.
- Smart, K. J., Ofoegbu, G. I., Morris, A. P., McGinnis, R. N., and Ferrill, D. A.: Geomechanical modeling of hydraulic fracturing: Why mechanical stratigraphy, stress state, and pre-existing structure matter, *AAPG Bulletin*, 98, 2237–2261, <https://doi.org/10.1306/07071413118>, 2014.
- 830 Sonder, L. J.: Effects of density contrasts on the orientation of stresses in the lithosphere: Relation to principal stress directions in the Transverse Ranges, California, *Tectonics*, 9, 761–771, <https://doi.org/10.1029/TC009i004p00761>, 1990.
- Stephansson, O. and Ångman, P.: Hydraulic Fracturing Stress Measurements At Forsmark and Stidsvig, Sweden., *Bulletin of the Geological Society of Finland*, pp. 307–333, <https://doi.org/10.17741/bgsf/58.1.021>, 1986.
- 835 Su, S. and Stephansson, O.: Effect of a fault on in situ stresses studied by the distinct element method, *International Journal of Rock Mechanics and Mining Sciences*, 36, 1051–1056, [https://doi.org/10.1016/S1365-1609\(99\)00119-7](https://doi.org/10.1016/S1365-1609(99)00119-7), 1999.
- Tamagawa, T. and Pollard, D. D.: Fracture permeability created by perturbed stress fields around active faults in a fractured basement reservoir, *AAPG Bulletin*, 92, 743–764, <https://doi.org/10.1306/02050807013>, 2008.
- 840 Tenthorey, E. and Cox, S. F.: Cohesive strengthening of fault zones during the interseismic period: An experimental study, *Journal of Geophysical Research: Solid Earth*, 111, 1–14, <https://doi.org/10.1029/2005JB004122>, 2006.
- Tesauro, M., Kaban, M. K., and Cloetingh, S.: Global strength and elastic thickness of the lithosphere, *Global and Planetary Change*, 90–91, 51–57, <https://doi.org/10.1016/j.gloplacha.2011.12.003>, 2012.

- Tingay, M. R., Müller, B., Reinecker, J., and Heidbach, O.: State and origin of the present-day stress field in sedimentary basins: New results
845 from the world stress map project, in: Proceedings of the 41st U.S. Rock Mechanics Symposium - ARMA's Golden Rocks 2006 - 50 Years
of Rock Mechanics, 41, p. 14, American Rock Mechanics Association, Golden, Colorado, [https://www.onepetro.org/conference-paper/
ARMA-06-1049](https://www.onepetro.org/conference-paper/ARMA-06-1049), 2006.
- Tommasi, A., Vauchez, A., and Daudré, B.: Initiation and propagation of shear zones in a heterogeneous continental lithosphere, *Journal of
Geophysical Research: Solid Earth*, 100, 22 083–22 101, <https://doi.org/10.1029/95JB02042>, 1995.
- 850 Torabi, A. and Berg, S. S.: Scaling of fault attributes: A review, *Marine and Petroleum Geology*, 28, 1444–1460,
<https://doi.org/10.1016/j.marpetgeo.2011.04.003>, 2011.
- Trefffeisen, T. and Henk, A.: Elastic and frictional properties of fault zones in reservoir-scale hydro-mechanical models-a sensitivity study,
Energies, 13, 25–27, <https://doi.org/10.3390/en13184606>, 2020a.
- Trefffeisen, T. and Henk, A.: Representation of faults in reservoir-scale geomechanical finite element models – A comparison of different
855 modelling approaches, *Journal of Structural Geology*, 131, 103 931, <https://doi.org/10.1016/j.jsg.2019.103931>, 2020b.
- van den Ende, M. P. A. and Niemeijer, A. R.: An investigation into the role of time-dependent cohesion in interseismic fault restrengthening,
Scientific Reports, 9, 1–11, <https://doi.org/10.1038/s41598-019-46241-5>, 2019.
- Wang, C., Song, C., Guo, Q., Mao, J., and Zhang, Y.: New insights into stress changes before and after the Wenchuan Earthquake using
hydraulic fracturing measurements, *Engineering Geology*, 194, 98–113, <https://doi.org/10.1016/j.enggeo.2015.05.016>, 2015.
- 860 Xing, H. L., Makinouchi, A., and Mora, P.: Finite element modeling of interacting fault systems, *Physics of the Earth and Planetary Interiors*,
163, 106–121, <https://doi.org/10.1016/j.pepi.2007.05.006>, 2007.
- Yale, D. P.: Fault and stress magnitude controls on variations in the orientation of in situ stress, *Geological Society Special Publication*, 209,
55–64, <https://doi.org/10.1144/GSL.SP.2003.209.01.06>, 2003.
- Yoon, J. S., Zang, A., and Stephansson, O.: Numerical investigation on optimized stimulation of intact and naturally frac-
865 tured deep geothermal reservoirs using hydro-mechanical coupled discrete particles joints model, *Geothermics*, 52, 165–184,
<https://doi.org/10.1016/j.geothermics.2014.01.009>, 2014.
- Yoon, J. S., Stephansson, O., Zang, A., Min, K. B., and Lanaro, F.: Discrete bonded particle modelling of fault activation near a nuclear waste
repository site and comparison to static rupture earthquake scaling laws, *International Journal of Rock Mechanics and Mining Sciences*,
98, 1–9, <https://doi.org/10.1016/j.ijrmms.2017.07.008>, 2017.
- 870 Zhang, S. and Ma, X.: How Does In Situ Stress Rotate Within a Fault Zone? Insights From Explicit Modeling of the Frictional, Fractured
Rock Mass, *Journal of Geophysical Research: Solid Earth*, 126, 1–23, <https://doi.org/10.1029/2021JB022348>, 2021.
- Zhang, Y., Clennell, M. B., Delle Piane, C., Ahmed, S., and Sarout, J.: Numerical modelling of fault reactivation in carbonate
rocks under fluid depletion conditions – 2D generic models with a small isolated fault, *Journal of Structural Geology*, 93, 17–28,
<https://doi.org/10.1016/j.jsg.2016.10.002>, 2016.
- 875 Zhou, C., Yin, J., Luo, J., and Xiao, G.: Law of geo-stress distribution in the vicinity of fault zone, *Journal of Yangtze River Scientific
Research Institute*, 29, 57–61, <https://doi.org/10.3969/j.issn.1001-5485.2012.07.013>, 2012.
- Zoback, M., Hickman, S., and Ellsworth, W.: Scientific drilling into the San Andreas fault zone - An overview of SAFOD's first five years,
Scientific Drilling, pp. 14–28, <https://doi.org/10.2204/iodp.sd.11.02.2011>, 2011.
- Zoback, M. D.: *Reservoir Geomechanics*, Cambridge University Press, <https://doi.org/10.1017/CBO9780511586477>, 2010.

880 Zoback, M. D., Zoback, M.-L., Mount, V. S., Suppe, J., Eaton, J. P., Healy, J. H., Oppenheimer, D., Reasenber, P., Jones, L., Raleigh, C. B., Wong, I. G., Scotti, O., and Wentworth, C.: New Evidence on the State of Stress of the San Andreas Fault System, *Science*, 238, 1105–1111, <https://doi.org/10.1126/science.238.4830.1105>, 1987.

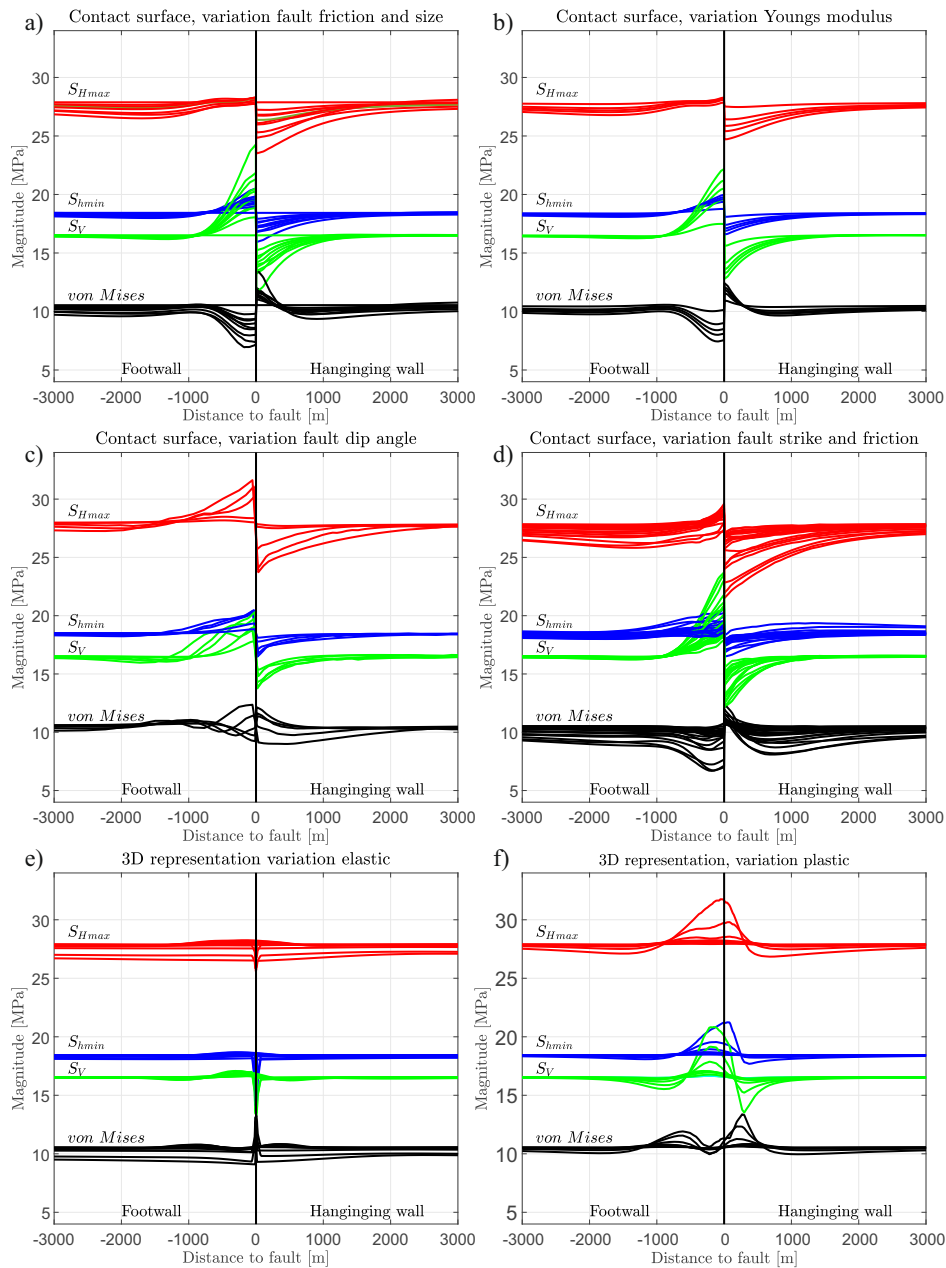


Figure 24. Summary illustration of the results from various presented models. Subfigure a) shows the impact of the fault friction ($\mu = 0.1, 0.2, 0.4, 0.6, 1.0$ and > 1.0) using contact elements (Fig. 8) and the influence of the fault size and model size (Fig. 22), b) displays the influence of a variable Young's modulus of the host rock on the stress state near and far the fault (Fig. 20). Subfigure c) shows the impact of a variable fault dip (Figs. 15 and 16), where d) illustrates the impact of a variable fault strike and additionally friction variation ($\mu = 0.1, 0.2, 0.3$ and 0.4) on the stress state resulting from a fault represented by a contact surface (Figs. 16, 17, 15 and 17, 18), where d) illustrates the influence of the fault size and model size (Fig. 22). The impact of a fault representation by 3-D elements is shown, where e) elastically weak elements are with a different stiffness (Figs. 10 and 11) and e) where the elements are allowed to plasticify as a result of a variable low friction (Fig. 14) and a laterally variable amount of elements (Fig. 13).

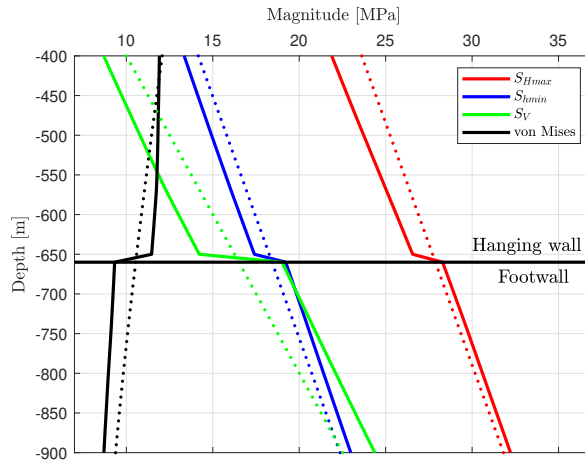


Figure 25. Stress magnitudes from a virtual well section for the depth range of 400 to 900 m depth, of the reference model having contact surfaces (continuous line) and a model without a fault (dotted line).

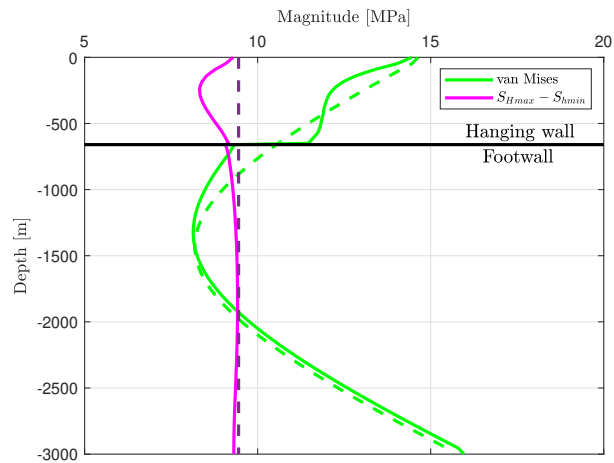


Figure 26. The von Mises and the difference between both horizontal stresses ($S_{Hmax} - S_{Hmin}$) are shown for the reference model with contact surfaces (continuous line) and a model with a continuous mesh (dotted line).